

AD-A248 292



2

TECHNICAL REPORT BRL-TR-3321

BRL

MODIFIED POINT MASS TRAJECTORY SIMULATION
FOR BASE-BURN PROJECTILES

R. F. LIESKE
J. E. DANBERG

DTIC
SELECTE
APR 6 1992
S B D

MARCH 1992

APPROVED FOR PUBLIC RELEASE; DISTRIBUTION IS UNLIMITED.

U.S. ARMY LABORATORY COMMAND

BALLISTIC RESEARCH LABORATORY
ABERDEEN PROVING GROUND, MARYLAND

92 4 03 200

92-08678



NOTICES

Destroy this report when it is no longer needed. DO NOT return it to the originator.

Additional copies of this report may be obtained from the National Technical Information Service, U.S. Department of Commerce, 5285 Port Royal Road, Springfield, VA 22161.

The findings of this report are not to be construed as an official Department of the Army position, unless so designated by other authorized documents.

The use of trade names or manufacturers' names in this report does not constitute indorsement of any commercial product.

REPORT DOCUMENTATION PAGE

Form Approved
OMB No. 0704-0188

Public reporting burden for this collection of information is estimated to average 1 hour per response, including the time for reviewing instructions, searching existing data sources, gathering and maintaining the data needed, and completing and reviewing the collection of information. Send comments regarding this burden estimate or any other aspect of the collection of information, including suggestions for reducing this burden, to Washington Headquarters Services, Directorate for Information Operations and Reports, 1215 Jefferson Davis Highway, Suite 1204, Arlington, VA 22202-4302, and to the Office of Management and Budget, Paperwork Reduction Project (0704-0188), Washington, DC 20503.

1. AGENCY USE ONLY (Leave blank)	2. REPORT DATE	3. REPORT TYPE AND DATES COVERED Final, Sep 90-Dec 91	
4. TITLE AND SUBTITLE Modified Point Mass Trajectory Simulation for Base-Burn Projectiles		5. FUNDING NUMBERS PR: 1L162618AH80	
6. AUTHOR(S) R. F. Lieske and J. E. Danberg			
7. PERFORMING ORGANIZATION NAME(S) AND ADDRESS(ES)		8. PERFORMING ORGANIZATION REPORT NUMBER	
9. SPONSORING / MONITORING AGENCY NAME(S) AND ADDRESS(ES) U.S. Army Ballistic Research Laboratory ATTN: SLCBR-DD-T Aberdeen Proving Ground, MD 21005-5066		10. SPONSORING / MONITORING AGENCY REPORT NUMBER BRL-TR-3321	
11. SUPPLEMENTARY NOTES			
12a. DISTRIBUTION / AVAILABILITY STATEMENT Approved for public release; distribution is unlimited.		12b. DISTRIBUTION CODE	
13. ABSTRACT (Maximum 200 words) An addition to the Modified Point Mass Trajectory Model for Rocket-Assisted Projectiles is presented for the exterior ballistic simulation of base-burn projectiles. The addition models the change in aerodynamic base-drag based on the change in base pressure due to the base-burn motor's ejection of hot gas into the wake of the projectile. The mass flow rate of the remaining fuel of the base-burn motor is modeled as a function of the instantaneous projectile spin rate and atmospheric air pressure. HAWK Doppler radar data collected at Yuma Proving Ground, Arizona, for the 155mm, M1864 base-burn projectile have been used to verify the modeling approach for a variety of test conditions.			
14. SUBJECT TERMS Base-Burn Projectile, Trajectory Modeling, Doppler Radar, Aerodynamic Drag			15. NUMBER OF PAGES
			16. PRICE CODE
17. SECURITY CLASSIFICATION OF REPORT UNCLASSIFIED	18. SECURITY CLASSIFICATION OF THIS PAGE UNCLASSIFIED	19. SECURITY CLASSIFICATION OF ABSTRACT UNCLASSIFIED	20. LIMITATION OF ABSTRACT SAR

INTENTIONALLY LEFT BLANK.

TABLE OF CONTENTS

	<u>Page</u>
LIST OF FIGURES	v
LIST OF TABLES	vi
ACKNOWLEDGMENTS	vii
1. INTRODUCTION	1
2. PHYSICS OF BASE-BURN PROJECTILES	1
3. DETERMINATION OF AERODYNAMIC DRAG FROM DOPPLER RADAR DATA (Lieske 1989)	3
4. MODELING THE BASE-BURN PROJECTILE DRAG	6
5. MODELING THE BASE-BURN MOTOR MASS FLOW RATE	6
6. ANALYSIS OF RESULTS	7
6.1 Modeled Mass Flow Rate of the Fuel	8
6.2 Change in Base Pressure	8
6.3 Deduced Mass Flow Rate of the Fuel	9
7. TRAJECTORY MODEL FOR ROCKET-ASSISTED AND BASE-BURN PROJECTILES	10
7.1 Equations of Motion	11
7.1.1 Thrust.	11
7.1.2 Drag Reduction.	11
7.2 Mass Flow Rate	11
7.3 Center of Mass	12
7.4 Axial Moment of Inertia	12
7.5 Overturning Moment Coefficient	13
7.6 Fitting Factors for Motor Performance	13
8. CONCLUSIONS	14
9. REFERENCES	29
LIST OF SYMBOLS	31
DISTRIBUTION LIST	35



iii

Accession For	
NTIS GRA&I	<input checked="" type="checkbox"/>
LTIC TAB	<input type="checkbox"/>
Unannounced	<input type="checkbox"/>
Justification _____	
By _____	
Distribution/ _____	
Availability Codes	
Dist	Avail and/or Special
A-1	

INTENTIONALLY LEFT BLANK.

LIST OF FIGURES

<u>Figure</u>		<u>Page</u>
1	Change in Base Pressure for a Change in Injection Parameter vs. Mach Number for Low Injection Rates and Temperatures from Wind Tunnel and CFD Results (Danberg 1990)	15
2	Change in Base Pressure vs. Injection Parameter for Various Mach Numbers Based on CFD Computations	15
3	Change in Base Pressure for a Change in Injection Parameter vs. Mach Number for Low Injection Rates and Various Temperatures Based on CFD Computations (Danberg 1990)	16
4	Change in Base Pressure for a Change in Injection Parameter vs. Mach Number for Various Injection Parameters Based on CFD Computations	16
5	Physical Characteristics of the 155mm, DPICM, M864 Projectile	17
6	155mm, DPICM, M864 Motor	18
7	155mm, DPICM, M864 Motor Propellant Grain	18
8	Aerodynamic Drag Force Coefficient for the 155mm, DPICM, M864 Projectile with an Inert Motor Propellant Grain (Lieske 1989)	19
9	Experimental Strand Burning Rate for M864 Motor Propellant (Miller and Holmes 1987)	19
10	Change in Base Pressure for a Change in Injection Parameter vs. Mach Number and Injection Parameter for the M864 Projectile	20
11	Reference Mass Flow Rate of the Fuel as a Function of the Pseudo-Time-of-Flight for the M864 Motor	20
12	Deduced and Modeled Mass Flow Rate vs. Time-of-Flight for Round Number 5089 Fired with Propelling Charge M4A2, 7W, at a Quadrant Elevation of 500 Mils	21
13	Deduced and Modeled Mass Flow Rate vs. Time-of-Flight for Round Number 1034 Fired with Propelling Charge M4A2, 7W, at a Quadrant Elevation of 750 Mils	21
14	Deduced and Modeled Mass Flow Rate vs. Time-of-Flight for Round Number 1013 Fired with Propelling Charge M4A2, 7W, at a Quadrant Elevation of 1150 Mils	22
15	Deduced and Modeled Mass Flow Rate vs. Time-of-Flight for Round Number 1044 Fired with Propelling Charge M119A2, 7R, at a Quadrant Elevation of 500 Mils	22

LIST OF FIGURES (Continued)

<u>Figure</u>		<u>Page</u>
16	Deduced and Modeled Mass Flow Rate vs. Time-of-Flight for Round Number 1050 Fired with Propelling Charge M119A2, 7R, at a Quadrant Elevation of 750 Mils	23
17	Deduced and Modeled Mass Flow Rate vs. Time-of-Flight for Round Number 4202 Fired with Propelling Charge M119A2, 7R, at a Quadrant Elevation of 1150 Mils	23
18	Deduced and Modeled Mass Flow Rate vs. Time-of-Flight for Round Number 4216 Fired with Propelling Charge M203E2, 8R, at a Quadrant Elevation of 499 Mils	24
19	Deduced and Modeled Mass Flow Rate vs. Time-of-Flight for Round Number 4329 Fired with Propelling Charge M203E2, 8R, at a Quadrant Elevation of 748 Mils	24
20	Deduced and Modeled Mass Flow Rate vs. Time-of-Flight for Round Number 4219 Fired with Propelling Charge M203E2, 8R, at a Quadrant Elevation of 1147 Mils	25
21	Difference Between Deduced and Modeled Mass Flow Rate ($\Delta\dot{m}_f$) vs. Pseudo-Time-of-Motor Burning	25
22	Difference Between Deduced and Modeled Mass Flow Rate ($\Delta\dot{m}_f$) vs. Mach Number	26
23	Difference Between Deduced and Modeled Mass Flow Rate ($\Delta\dot{m}_f$) vs. Injection Parameter	26
24	Difference Between Deduced and Modeled Mass Flow Rate ($\Delta\dot{m}_f$) vs. Projectile Spin Rate	27
25	Difference Between Deduced and Modeled Mass Flow Rate ($\Delta\dot{m}_f$) vs. Local Atmospheric Air Pressure	27
26	Difference Between Deduced and Modeled Mass Flow Rate ($\Delta\dot{m}_f$) vs. Time-of-Flight	28

LIST OF TABLES

<u>Table</u>		<u>Page</u>
1	Experimental Spin Fixture Time-to-Burnout for the M864 Motor (Kayser, Kuzan, and Vazquez 1987)	8
2	Fitting Factors for Rocket-Assisted and Base-Burn Motor Performance	13

ACKNOWLEDGMENTS

The authors would like to express their appreciation to Mr. Joseph A. Hurff for preparing the computer programs required to calculate the aerodynamic drag results and to Mr. Richard C. Eitemiller for assembling and reducing the 155mm, DPICM, M864 base-burn projectile experimental range firing data. The authors would also like to express their appreciation to COL Didrik Cappelen (Norway), Prof. E. Celens (Belgium), and Messrs. James W. Bradley and James A. Matts for their very helpful comments and suggestions during the preparation and review of this report.

INTENTIONALLY LEFT BLANK.

1. INTRODUCTION

The Modified Point Mass Trajectory Model (Lieske and Reiter 1966 and NATO Army Armaments Group STANAG 4355, 1988) is the primary method of trajectory simulation used in the preparation of Firing Tables. This model requires four types of input data: projectile mass properties, motor characteristics, aerodynamic coefficients, and the performance parameters determined from experimental range testing. This report presents a method of modeling the aerodynamic drag of base-burn projectiles with as much similarity as possible to the approach used for rocket-assisted projectiles. HAWK Doppler radar data for the 155mm, Dual Purpose Improved Conventional Munition (DPICM), M864 base-burn projectile have been analyzed and used to verify the modeling approach for a variety of test conditions. The word "deduced," as used in this report, means a computed value based on an analysis of the measured Doppler radar data; all symbols are defined in the List of Symbols.

2. PHYSICS OF BASE-BURN PROJECTILES

Theoretical discussions of the mechanism of base drag reduction for base-burn projectiles are presented in the works of Gunners, Andersson and Hellgren, Chapter 16 (1988) and Danberg (1990). In these works, it is assumed that mass injection into the near wake only affects the pressure distribution on the projectile base and thus only affects the base drag. Forebody pressure and viscous drag are unaffected. As a result, the drag coefficient of a base-burn projectile can be considered to be equal to the drag coefficient of the non-burning (inert) projectile, C_{D_0} , minus the difference in the base drag component, $\Delta C_{D_{0bb}}$, between an inert and operating base-burn motor. The base drag component of a projectile, C_{D_b} , is directly related to the average projectile base pressure, P_b , as follows:

$$C_{D_b} = \frac{1 - \frac{P_b}{P}}{\frac{\gamma}{2} M^2 \frac{1}{d_b^2}} \quad (1)$$

where:

- d_b = base diameter of projectile in calibers
- M = local flight Mach number
- P = local atmospheric air pressure
- P_b = average projectile base pressure
- γ = ratio of specific heats

From this relationship, the theoretical difference in the base drag component for a projectile with an inert base-burn motor (average base pressure, P_{bi}) and an operating base-burn motor (average base pressure, P_{bb}) can be written as:

$$\Delta C_{D_{0bb}} = \frac{\frac{P_{bb}}{P} - \frac{P_{bi}}{P}}{\frac{\gamma}{2} M^2 \frac{1}{d_b^2}} \quad (2)$$

The overall drag coefficient of a base-burn projectile with an operating base-burn motor is then:

$$C_{D_{0bb}} = C_{D_0} - \Delta C_{D_{0bb}} \quad (3)$$

In subsequent sections of this report, the difference in the average base pressure ratios $\left(\frac{P_{bb}}{P} - \frac{P_{bi}}{P}\right)$ will be designated ΔBP .

The nondimensional injection parameter I is defined as:

$$I = \frac{\dot{m}_f}{\rho v A_b} \quad (4)$$

where \dot{m}_f is the injected mass flow and $\rho v A_b$ is the free-stream mass flow through an area equal to the base of the projectile, A_b . Danberg (1990) has shown that ΔBP is linearly related to I over a range of low rates of air injection (I less than 0.005 at M less than 2.5 and at 300 K temperature) as observed in a number of wind tunnel experiments:

$$\Delta BP = I \left[\frac{\delta(P_{bb}/P)}{\delta I} \right]_{I=0} \quad (5)$$

The slope $\left[\frac{\delta(P_{bb}/P)}{\delta I} \right]_{I=0}$ in Equation 5 was found to depend only on the free-stream

Mach number for the wind tunnel data; see Figure 1 which is from Danberg (1990). Using computational fluid dynamics (CFD), Nietubicz and Sahu (1988) confirmed the low-temperature results (approximately 300 K) and extended them to more realistic temperatures consistent with burning of a solid propellant. They numerically solved the Navier-

Stokes equations for the flow around the M864 projectile, including its domed base, for a wide range of injection mass flows and gas temperatures. Figure 2 indicates the general form of the average base pressure change with increasing injection parameter for Mach numbers from 1.3 to 3.0. The data points are the computed CFD values corresponding to a stagnation temperature of the injected gas of 1500 K. Note that these curves can also be represented by a line through the origin with a slope that increases with Mach number for injection rates of less than 0.002. This slope has been computed for a range of Mach numbers and injected gas temperatures and is shown in Figure 3 along with the low-temperature data from Figure 1. The lines drawn through the data points are computed from an equation fitted to the CFD data. The equation is a cubic polynomial in Mach number with coefficients that are linear in the injected gas temperature, T_j . The data of Figure 3 are valid for injection rates of less than 0.002.

At higher injection rates, the base pressure difference is no longer linear with respect to I ; Figure 2 illustrates this. However, ΔBP can be represented in terms of a new variable made up of the product of the injection rate and the slope.

In applying these results to flight test data, ΔBP is assumed to have the form:

$$\Delta BP = I \left(\frac{\delta BP}{\delta I} \right) \quad (6)$$

where for low injection rates and a fixed gas temperature, $\frac{\delta BP}{\delta I}$ approaches the limiting slopes shown in Figure 3. For a specific propellant, the limit is expected to be only a function of Mach number. For larger values of I , a decrease of $\frac{\delta BP}{\delta I}$ with I corresponds to a nonlinear curve of base pressure change. The CFD data can be used to provide an estimate of the decrease in $\frac{\delta BP}{\delta I}$ for fixed values of I , as shown in Figure 4.

3. DETERMINATION OF AERODYNAMIC DRAG FROM DOPPLER RADAR DATA (Lieske 1989)

Doppler radar is one of the most valuable tools in evaluating the aerodynamic drag of projectiles from full-scale flight tests. The basis of the data reduction is the relationship between the measured time rate of change of slant range and the projectile acceleration. The

technique is developed in a ground-fixed, orthonormal, right-handed Cartesian coordinate system with unit vectors ($\vec{1}$, $\vec{2}$ and $\vec{3}$). The $\vec{1}$ axis is the intersection of the vertical plane of fire and the horizontal plane and points in the direction of fire. The $\vec{2}$ axis is parallel to the gravity vector, \vec{g} , and opposite in direction. The $\vec{3}$ axis completes the right-handed coordinate system.

The slant range rate of change as measured by Doppler radar is recorded on magnetic tape. The first step is to smooth the data and determine the time derivative. Least squares fits (second-degree polynomials in time) to the data are determined for 0.56 second intervals (fifteen point smoothing) along the trajectory. The slant range rate of change (\dot{r}) and time derivative of the slant range rate of change (\ddot{r}) are obtained from the quadratic fit at the midpoint of the fifteen-point interval.

An estimated trajectory for the base-burn projectile is generated separately using the projectile mass properties, launch data, atmospheric conditions, estimated aerodynamic coefficients, and estimated drag reduction while the base-burn motor is operating. The trajectory is adjusted, using factors on both the drag reduction during motor functioning and lift, to match the observed impact data. A trajectory velocity (\vec{u}_r) is calculated using the Doppler radar smoothed slant range rate of change (\dot{r}) and the estimated trajectory slant range rate of change (\dot{r}_t) and velocity (\vec{u}_t) as follows:

$$\vec{u}_r = (\dot{r} / \dot{r}_t) \vec{u}_t \quad (7)$$

where:

$$\dot{r}_t = u_t \cos(r_t, u_t) = (\vec{r}_t \cdot \vec{u}_t) / r_t$$

A trajectory acceleration ($\dot{\vec{u}}_r$) was calculated using the time derivative of the Doppler radar slant range rate of change (\ddot{r}) and the estimated trajectory time derivative of the slant range rate of change (\ddot{r}_t) and acceleration ($\dot{\vec{u}}_t$), utilizing the following two formulations:

$$\dot{\vec{u}}_r = (\dot{r} / \dot{r}_t) \dot{\vec{u}}_t + [(\dot{r}_t \ddot{r} - \dot{r} \ddot{r}_t) / \dot{r}_t^2] \vec{u}_t \quad (8)$$

and

$$\dot{\vec{u}}_r = (\ddot{r} / \ddot{r}_t) \dot{\vec{u}}_t \quad (9)$$

where:

$$\vec{r}_t = \{ r_t [(\dot{\vec{r}}_t \cdot \vec{u}_t) + (\vec{r}_t \cdot \dot{\vec{u}}_t)] - (\vec{r}_t \cdot \vec{u}_t) \vec{r}_t \} / r_t^2$$

and

$$\dot{\vec{r}}_t = \vec{u}_t$$

The mean of the results were similar for both of the \vec{u}_r representations; however, the variation (spread) of the results were significantly improved using Equation 9 and it was used for determining the results presented.

Note: Subscript t refers to quantities determined from the estimated trajectory and those with subscript r are obtained using both the Doppler radar data and the estimated trajectory.

The mass of the projectile, atmospheric conditions, estimated trajectory data and the Doppler slant range rate of change and its time derivative provide the necessary inputs to determine the aerodynamic drag. The following inverse solution of the point-mass equations of motion is then used to compute the aerodynamic drag (C_{D_r}).

$$C_{D_r} = - [(\vec{u}_r - \vec{w}) \bullet (\dot{\vec{u}}_r - \vec{g} - \vec{\Lambda})] 8 m / (\pi \rho d^2 v^3) \quad (10)$$

This equation can be used to experimentally determine the aerodynamic drag coefficient for a projectile with either an inert or a functioning base-burn motor. The ΔBP for a particular flight condition can then be determined from the difference in the drag coefficient for projectiles with inert and operating base-burn motors. Based on the known flight conditions of projectile spin and atmospheric air pressure, the flight mass flow rate can be related to the mass flow generated by the gas generator for a set of reference conditions. This relationship will be discussed in sections 5 and 6. A deduced mass flow rate can be calculated using an estimated change in nondimensional base pressure for a change in the injection parameter based on the expected motor-ejected gas temperature and compared with the computed flight mass flow rate. The results can then be analyzed to refine the estimated mass flow rate and the change in nondimensional base pressure for a change in the injection parameter due to the base-burn motor ejecting hot gas into the wake of the projectile.

4. MODELING THE BASE-BURN PROJECTILE DRAG

The trajectory of a base-burn projectile is simulated by expanding the drag term, \vec{D} , in the Modified Point Mass Trajectory Model to include the change in drag due to the injection of a hot gas flow into the projectile's wake.

$$\vec{D} = -\frac{\pi \rho d^2 i}{8 m} \left\{ C_{D_0} - f_{BB} \left[\frac{\Delta BP}{\left(\frac{\gamma}{2}\right) M^2 \left(\frac{1}{d_0^2}\right)} \right] + C_{D_{\alpha^2}} (Q\alpha_e)^2 \right\} v \vec{v} \quad (11)$$

where $f_{BB} \left[\frac{\Delta BP}{\left(\frac{\gamma}{2}\right) M^2 \left(\frac{1}{d_0^2}\right)} \right]$ is used to represent the drag reduction due to the hot mass flow (\dot{m}_f) of the base-burn motor. The difference in drag due to the functioning of a base-burn motor is represented by a change in the projectile's base pressure (ΔBP) due to the nondimensional mass flow rate, I , as discussed in section 2, and the quantity:

$$\frac{\delta BP}{\delta I} = \mathcal{F}(M, I) \quad (12)$$

which can be deduced from the flight test data analysis. This assumes that the mass flow, which is a critical element, can adequately be modeled as a function of projectile spin and atmospheric air pressure as discussed in the next section. Finally, a factor f_{BB} is included for matching observed range firing data.

5. MODELING THE BASE-BURN MOTOR MASS FLOW RATE

The method used to determine the mass flow rate of the base-burn motor is an extension of the procedure used for rocket-assisted projectiles that is presented in NATO Army Armaments Group STANAG 4355.

The mass flow rate of the motor fuel, \dot{m}_f^* , as a function of pseudo-time-of-motor burning (t^*) is determined for a reference set of conditions of motor temperature, projectile spin rate, and atmospheric air pressure.

$$\dot{m}_f^* = \mathcal{F}(t^*) \quad (13)$$

A transformation from time-of-flight (t) to pseudo-time-of-motor burning t^* is used to determine the mass flow of the base-burn motor as a function of the currently predicted burn-out time, $t_{B(t+\Delta t)}$.

The effects of projectile spin rate and local atmospheric pressure conditions influence the mass flow through an estimated burnout time. The estimated burnout time, $t_{B(t+\Delta t)}$, assumes that the mass flow remains constant at the instantaneous conditions until the fuel is consumed. This burnout time is updated at each numerical integration time step and thus approaches the actual burnout time as the fuel is exhausted. The simulated burnout time is modeled by the following assumed formula:

$$t_{B(t+\Delta t)} = \left[(t_{B(t)} - t) \left(\frac{P(t+\Delta t)}{P(t)} \right)^{f_{BT_p}} \left(\frac{P(t+\Delta t)}{P(t)} \right)^{f_{BT_p}} \right] + t \quad (14)$$

where:

f_{BT_p} is a parameter used to represent the change in burning time of the motor due to projectile spin rate.

f_{BT_p} is a parameter used to represent the change in burning time of the motor due to a change in local atmospheric pressure.

and

$$t^*_{(t+\Delta t)} = t^*_{(t)} + \Delta t^* = t^*_{(t)} + \Delta t \left(\frac{t^*_B - t^*_{(t)}}{t_{B(t+\Delta t)} - t} \right) \quad (15)$$

Finally the instantaneous mass flow rate of the fuel is:

$$\dot{m}_f = \left(\frac{t^*_B - t^*_{(t)}}{t_{B(t+\Delta t)} - t} \right) \dot{m}^*_f \quad (16)$$

6. ANALYSIS OF RESULTS

A sample of nine 155mm, DPICM, M864 projectiles fired at quadrant elevations of approximately 500, 750 and 1150 mils with propelling charges: M4A2, charge 7W; M119A2, charge 7R; and M203E2, charge 8R were analysed. These projectiles were fired at Yuma Proving Ground, AZ, during May 1987. Figure 5 shows the configuration of the M864 pro-

jectile design and presents its physical properties. Figures 6 and 7 show the M864 base-burn motor, igniter, and grain. Figure 8 presents the aerodynamic drag for the M864 with an inert base-burn motor that was determined from HAWK Doppler radar data, for projectiles fired with inert base-burn motors as reported by Lieske (1989).

6.1 Modeled Mass Flow Rate of the Fuel. The mass flow rate for the M864 projectile is modeled using: (1) an estimated mass flow rate of the motor as a function of pseudo-time-of-flight for the reference spin rate, time-of-motor ignition, and time-of-motor burnout of 260 rev/s, 0.5 s, and 23.5 s, respectively; (2) the projectile spin burning rate factor, -0.50 , based on the experimentally measured time-to-burnout on a ground-mounted spin fixture (Kayser, Kuzan and Vazquez 1987), Table 1; (3) the experimentally determined strand pressure burning rate coefficient, converted to a burning time factor, -0.6655 , as reported by Miller and Holmes (1987), Figure 9; and (4) the computed change in base pressure for a change in injection parameter vs. Mach number, Figure 4.

Table 1. Experimental Spin Fixture Time-to-Burnout for the M864 Motor (Kayser, Kuzan, and Vazquez 1987).

Run Number	Spin (rev/s)	Burn-Time (s)
2	0	40.0
3	99	31.9
4	142	29.0
5	176	27.4
6	199	26.0
7	226	23.9
8	253	22.8

6.2 Change in Base Pressure. The change in nondimensional base pressure, ΔBP , due to the functioning base-burn motor is computed from the difference in aerodynamic drag between a projectile with an inert and a functioning base-burn motor as follows:

$$\Delta BP = \{C_{D_c} + [C_{D_{a2}} (Q \alpha_c)^2] - C_{D_r}\} \left(\frac{\gamma}{2}\right) M^2 \left(\frac{1}{d_b^2}\right) \quad (17)$$

6.3 Deduced Mass Flow Rate of the Fuel. The mass flow rate of the fuel, \dot{m}_f , is deduced using:

- a. the change in average base pressure due to the functioning motor;
- b. the change in nondimensional base pressure for a change in the base-burn motor injection parameter;
- c. the projectile base area;
- d. the projectile velocity; and
- e. the local atmospheric air pressure.

The firing propellant charge gases are supplemented by an igniter to ignite the solid propellant motor fuel; therefore, the igniter is considered part of the motor fuel.

$$\dot{m}_f = \frac{\rho v A_b \Delta BP}{\frac{\delta BP}{\delta I}} \quad (18)$$

The differences between the deduced mass flow rate based on the HAWK Doppler radar data and the modeled mass flow rate were determined for the M864 projectiles fired at quadrant elevations of approximately 500, 750, and 1150 mils with propelling charges: M4A2, charge 7W; M119A2, charge 7R; and M203E2, charge 8R. These differences were analyzed with respect to pseudo-time-of-flight, Mach number, injection parameter, local atmospheric pressure and time-of-flight. The analysis of the differences suggested a modification to the change in base pressure for a change in injection parameter, and the reference mass flow rate of the fuel. Therefore, an iterative procedure was used to simultaneously determine the change in base pressure for a change in injection parameter as a function of Mach number and injection parameter, and the reference mass flow rate of the fuel as a function of the pseudo-time-of-flight that would minimize the differences. The change in base pressure for a change in injection parameter as a function of Mach number and injection parameter, and the reference mass flow rate of the motor fuel as a function of the pseudo-time-of-flight that virtually minimized the differences are presented in Figures 10 and 11.

The results of this analysis indicated that the M864 base-burn motor requires a few seconds to ignite and reach full performance and has a reference motor burn-time of 24.0 seconds. The ignition delay, t_{DI} , of approximately 0.4 second has also been observed by Kuzan and Oskay (1988) during transonic range testing and the motor burn-time is within one second of the experimental ground-mounted time-to-burnout measurement by Kayser,

Kuzan and Vazquez (1987). The operating base-burn motor increases the maximum range of the M864 by approximately 18%. If the M864 motor igniter used to ignite the solid propellant motor fuel could be enlarged, it could also provide the mass flow of hot gases needed for drag reduction during the first few seconds and speed the ignition of the base-burn motor propellant. In that case, an increase in maximum range of approximately 20% could be achieved.

Figures 12 through 20 present the deduced and modeled mass flow rates vs. time of flight for projectiles fired with the three propelling charges at quadrant elevations of approximately 500, 750 and 1150 mils. The figures show an especially good correlation of the deduced with the modeled mass flow rate with time-of-flight for the propellant charge and quadrant elevation combinations with the various projectile spin rates and local atmospheric air pressures. One of the significant points to note is that the quality of agreement is about the same for all the conditions; this is despite the fact that the total burning time at the high quadrant elevations is more than twice that at the low quadrant elevations.

There is some irregularity in the results for the transonic velocity region (Mach numbers: .95 to 1.05). This is especially evident on Figure 12 for 15 to 20 seconds time-of-flight. The irregularity is probably due to the error in the transonic aerodynamic inputs and/or the Mach number determined from the HAWK Doppler radar data.

The difference between the deduced and modeled mass flow rate for the nine M864 base-burn test projectiles, shown in Figures 12 through 20, is presented in Figures 21 through 26 as functions of pseudo-time-of-motor burning, Mach number, injection parameter, local atmospheric air pressure, projectile spin rate and time-of-flight. The modeling process, using the experimentally determined inputs, provides a very good simulation of the exterior ballistic performance of the M864 based on the fact that the residuals show no systematic bias as a function of pseudo-time-of-motor burning, Mach number, injection parameter, local atmospheric air pressure, projectile spin rate and time-of-flight.

7. TRAJECTORY MODEL FOR ROCKET-ASSISTED AND BASE-BURN PROJECTILES

This section summarizes the equations that simulate the flight of rocket-assisted and base-burn projectiles. Both technologies are described, combining the common features of physical phenomena and providing a compact and flexible method for simulating these projectiles.

7.1 Equations of Motion. The equations of motion for rocket-assisted and base-burn projectiles are treated as a thrust and drag-reduction methodology, respectively. Thrust is defined as a force that produces an increase in total velocity (an acceleration) due to the functioning of a rocket motor; and drag-reduction is a reduction in drag (reduced deceleration) due to the functioning of a device such as base-burn motor, tracer, etc.

7.1.1 Thrust. The acceleration due to thrust, \vec{T} , of the rocket motor during burning ($t_{DI} \leq t \leq t_B$) is added to the equation of motion of the center of mass of the projectile:

$$\vec{T} = \left[\frac{f_T \dot{m}_f I_{SP} + (P_r - P) A_e}{m} \right] \left(\frac{\vec{v} \cos \alpha_e}{v} + \vec{\alpha}_e \right) \quad (19)$$

During rocket motor burning the aerodynamic zero-yaw drag coefficient is $C_{D_{0T}}$. The factor f_T is included for matching observed range firing data.

7.1.2 Drag Reduction. The base drag reduction due to a base-burn motor during burning ($t_{DI} \leq t \leq t_B$) is added to the drag term (\vec{D}) of the projectile:

$$\vec{D} = - \frac{\pi \rho d^2 i}{8 m} \left\{ C_{D_0} - f_{BB} \left[\frac{\left(\frac{\dot{m}_f}{\rho v A_b} \right) \left(\frac{\delta BP}{\delta I} \right)}{\left(\frac{\gamma}{2} \right) M^2 \left(\frac{1}{d_b^2} \right)} \right] + C_{D_{\alpha^2}} (Q \alpha_e)^2 \right\} v \vec{v} \quad (20)$$

where $f_{BB} \left[\frac{\left(\frac{\dot{m}_f}{\rho v A_b} \right) \left(\frac{\delta BP}{\delta I} \right)}{\left(\frac{\gamma}{2} \right) M^2 \left(\frac{1}{d_b^2} \right)} \right]$ is used to represent the drag reduction due to the mass flow (\dot{m}_f) of the base-burn motor. The factor f_{BB} is included for matching observed range firing data.

7.2 Mass Flow Rate. The mass flow is given by:

a. at $t = 0$:

$$m = m_0$$

$$\dot{m} = 0$$

b. for $t < t_{DI}$:

$$\dot{m} = - \frac{m_{DI}}{t_{DI}}$$

c. for $t_{DI} \leq t \leq t_B$:

$$\dot{m} = -\dot{m}_f$$

$$\dot{m}_f = \left(\frac{t_B^* - t_{(t)}^*}{t_{B(t+\Delta t)}^* - t} \right) \dot{m}_f$$

where:

$$t_{(t+\Delta t)}^* = \left(\frac{t_B^* - t_{(t)}^*}{t_{B(t+\Delta t)}^* - t} \right) \Delta t + t_{(t)}^*$$

where:

$$t_{B(t+\Delta t)}^* = \left[(t_{B(t)}^* - t) \left(\frac{p(t+\Delta t)}{p(t)} \right)^{f_{BTP}} \left(\frac{P(t+\Delta t)}{P(t)} \right)^{f_{BTP}} \right] + t$$

and at $t = t_{DI}$:

$$t_{(t)}^* = t_{DI}^*$$

$t_{B(t)}^*$ = Time-of-motor burnout for reference motor spin rate

$p(t)$ = Reference axial spin rate for motor mass flow (p_r)

$P(t)$ = Standard atmospheric air pressure (P_r)

d. for $t > t_B$:

$$m = m_0 - m_{DI} - m_f$$

$$\dot{m} = 0$$

7.3 Center of Mass. The location of the center of mass of the projectile is given by:

$$X_{CG} = X_{CG_0} + \left[\frac{(X_{CG_0} - X_{CG_B})(m - m_0)}{m_0 - m_B} \right] \quad (21)$$

7.4 Axial Moment of Inertia. The axial moment of inertia of the projectile is given by:

$$I_X = I_{X_0} + \left[\frac{(I_{X_0} - I_{X_B})(m - m_0)}{m_0 - m_B} \right] \quad (22)$$

7.5 Overturning Moment Coefficient. The overturning moment coefficient of the projectile is given by:

$$C_{M_\alpha} = C_{M_\alpha}^* + \left[\frac{(X_{CG} - X_{CG_0})(C_{D_{0T}} + C_{L_\alpha})}{d} \right] \quad (23)$$

where: $C_{M_\alpha}^*$ is determined for the initial projectile configuration.

7.6 Fitting Factors for Motor Performance. To compensate for the approximations in the rocket-assisted and base-burn motor performance terms, certain fitting factors contained in Table 2 are applied in order to create correspondence between the computed and the observed range testing results.

Table 2. Fitting Factors for Rocket-Assisted and Base-Burn Motor Performance.

Fitting	Fitting Function	
	Rocket-Assisted Projectiles	Base-Burn Projectiles
Change in Radial Velocity During Motor Burning	f_T A_e	$f_T = 0$ $A_e = 0$
Motor-burn Time	f_{BT}^* $f_{BT_P} = 0$	f_{BT} f_{BT_P}
Range	i $f_{BB} = 0$	$i = 1$ f_{BB}

* Optional

8. CONCLUSIONS

A methodology is presented to model the change in aerodynamic base-drag, based on the change in base pressure due to a base-burn motor injecting hot gas into the wake of a projectile. The procedure models the mass flow rate of the remaining fuel of the base-burn motor as a function of the instantaneous projectile spin rate and atmospheric air pressure. The modeling approach has been used to successfully simulate a variety of trajectories for the 155mm, DPICM, M864 base-burn projectile, based on the experimentally determined time-to-burnout and strand pressure burning rate results, and the HAWK Doppler radar data for experimental range firings.

The results of this analysis indicate that the M864 base-burn motor requires a few seconds to ignite and reach full performance. The maximum range of the M864 could be increased by approximately two percent if the igniter used to ignite the solid propellant motor fuel could also provide the mass flow of hot gases needed for drag reduction during the first few seconds and speed the base-burn motor propellant ignition process. Therefore, it is recommended that future base-burn motor designs consider this possibility.

The experimental results certainly support the proposed addition to the Modified Point Mass Trajectory Model for Rocket-Assisted Projectiles for the exterior ballistic simulation of the M864 base-burn projectile.

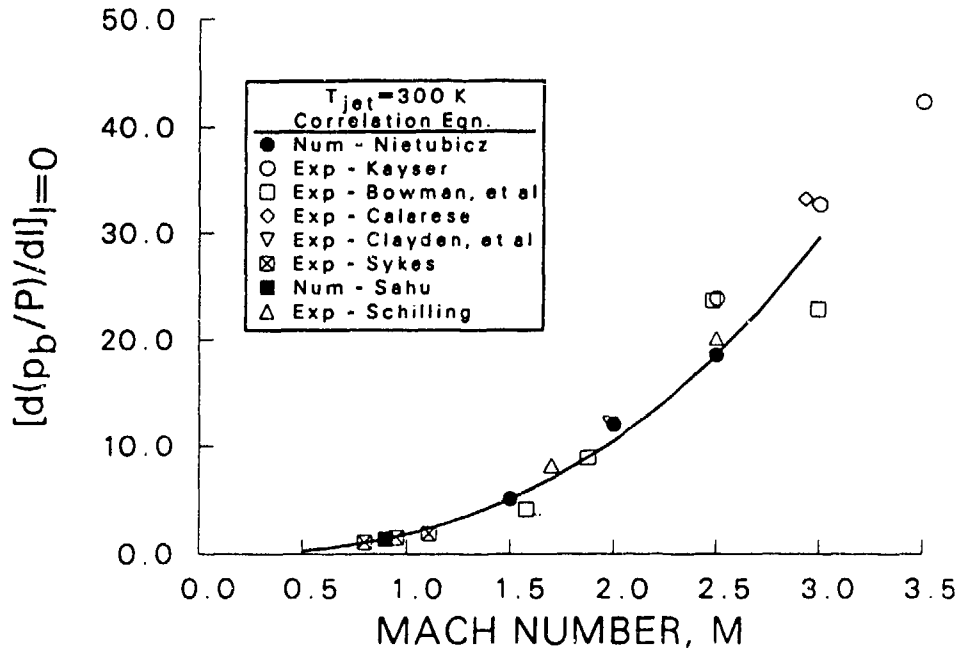


Figure 1. Change in Base Pressure for a Change in Injection Parameter vs. Mach Number for Low Injection Rates and Temperatures from Wind Tunnel and CFD Results (Danberg 1990).

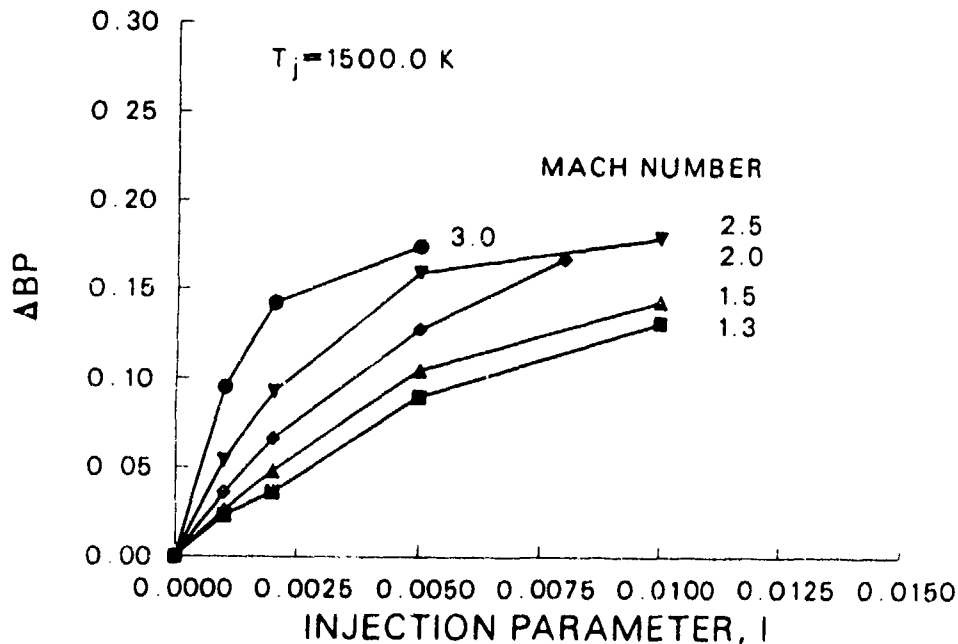


Figure 2. Change in Base Pressure vs. Injection Parameter for Various Mach Numbers Based on CFD Computations.

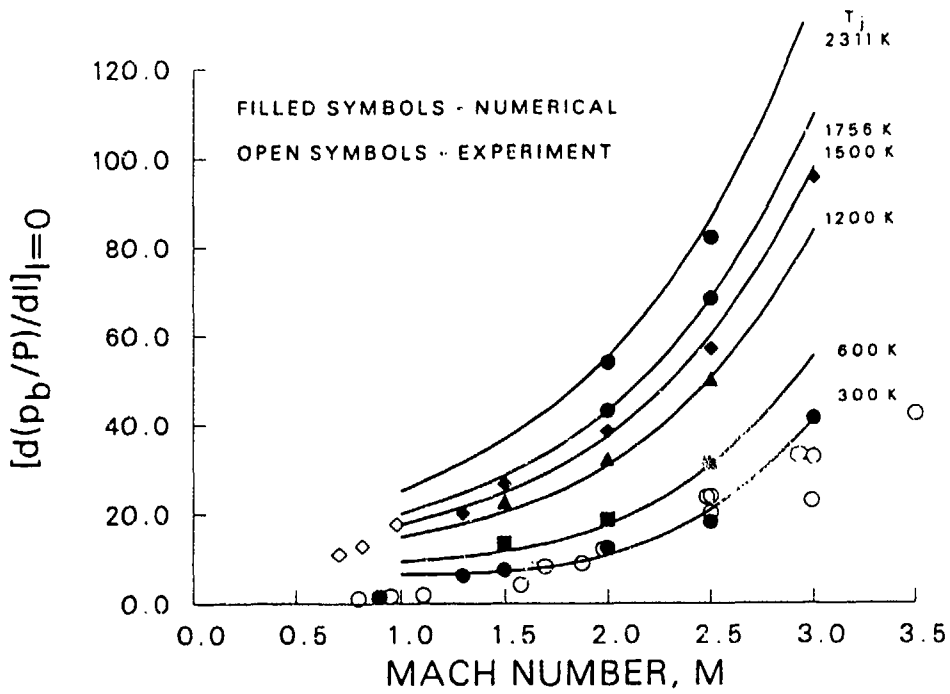


Figure 3. Change in Base Pressure for a Change in Injection Parameter vs. Mach Number for Low Injection Rates and Various Temperatures Based on CFD Computations (Danberg 1990).

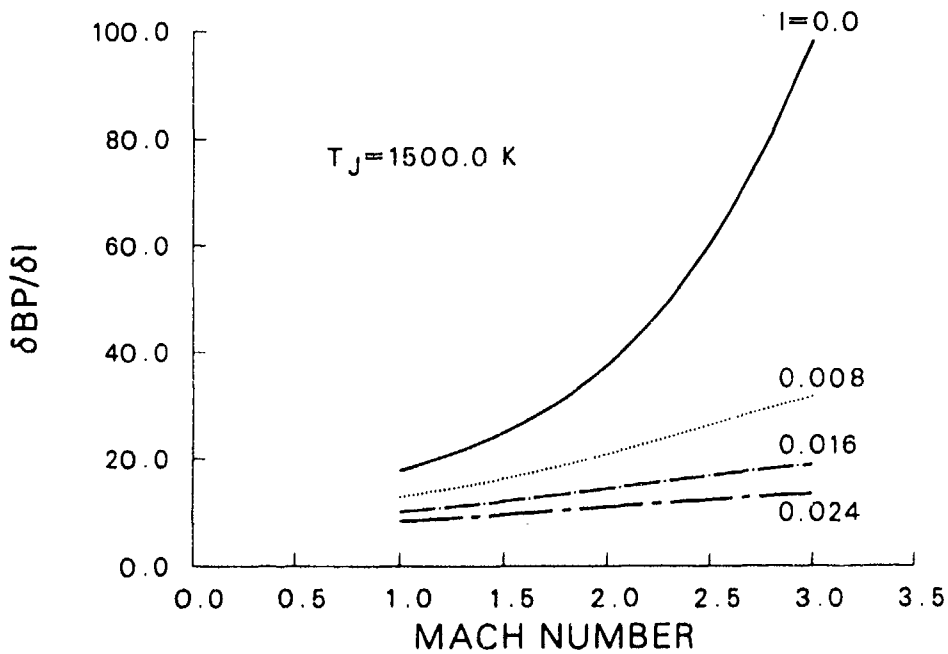
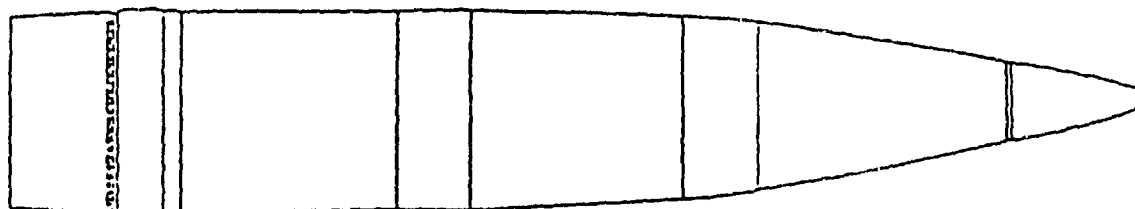


Figure 4. Change in Base Pressure for a Change in Injection Parameter vs. Mach Number for Various Injection Parameters Based on CFD Computations.

Projectile Sketch



Projectile Dimensions

Length of Projectile	calibers	5.79
Nose Length	calibers	3.42
Cylinder Length	calibers	1.86
Boattail Length	calibers	.50
Boattail Angle	degrees	3.00

Projectile Mass Properties

Mass	kgs	46.95
	(lbs)	103.5
Mass of Fuel	kgs	1.21
	(lbs)	2.67
Center of Gravity	cm from nose	58.8
	(inches from nose)	23.16
Moments of Inertia		
Axial	kg-m ²	.158
	(lb-ft ²)	3.75
Transverse	kg-m ²	1.657
	(lb-ft ²)	39.32

Figure 5. Physical Characteristics of the 155mm, DPICM, M864 Projectile.

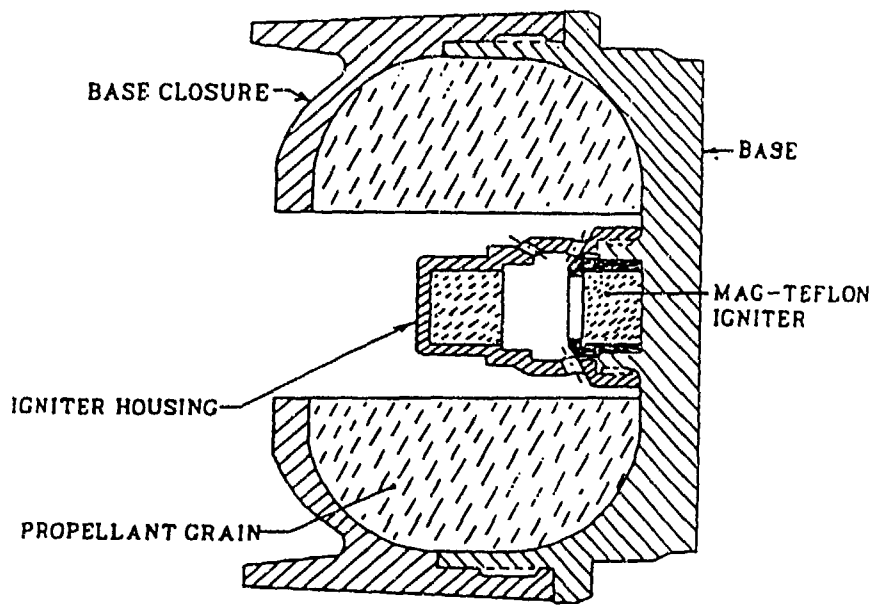
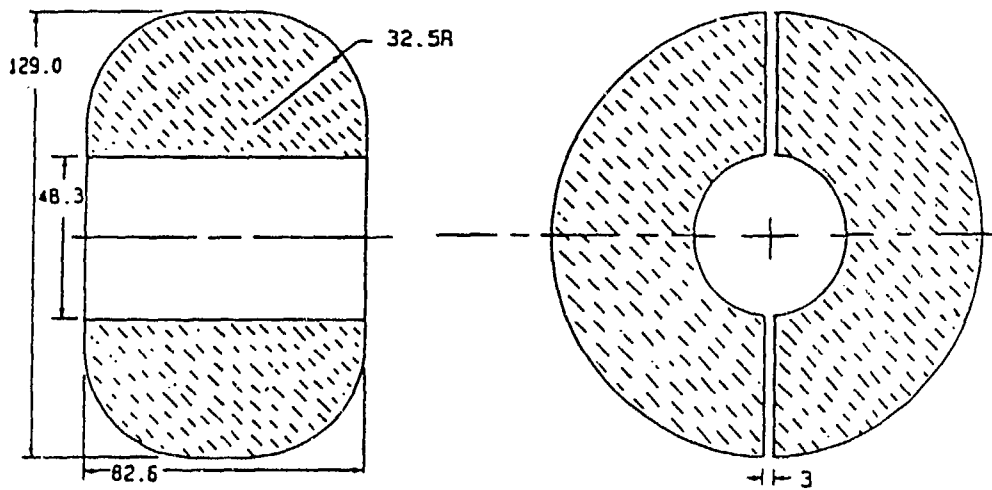


Figure 6. 155mm, DPICM, M864 Motor.



ALL DIMENSIONS IN MM

Figure 7. 155mm, DPICM, M864 Motor Propellant Grain.

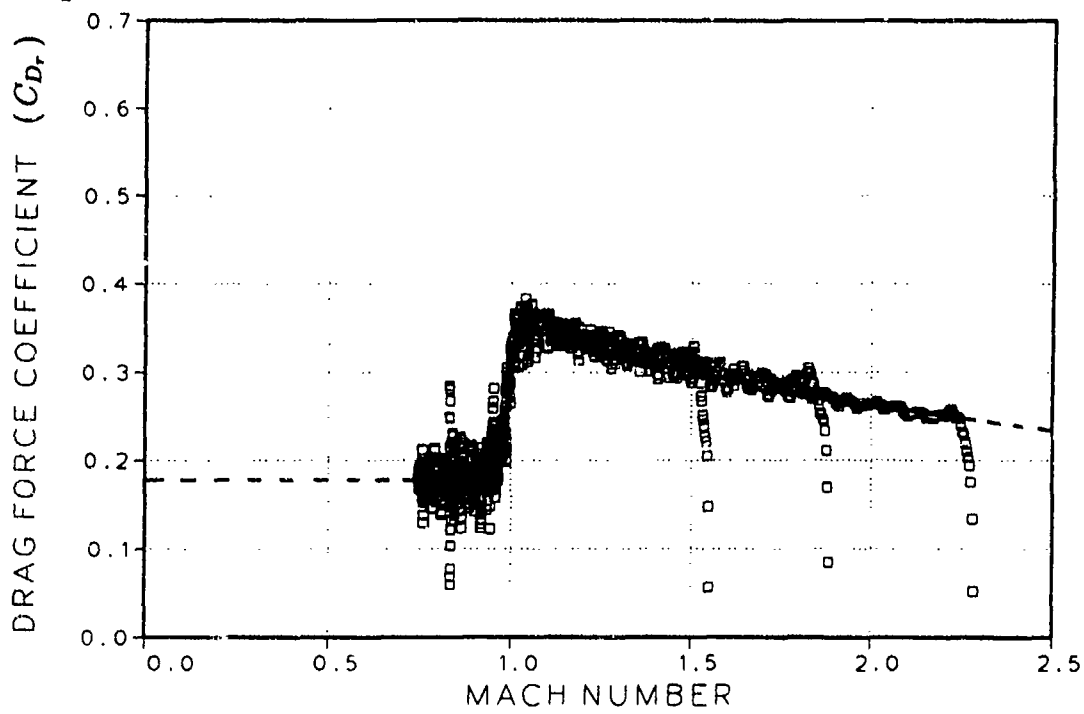


Figure 8. Aerodynamic Drag Force Coefficient for the 155mm, DPICM, M864 Projectile with an Inert Motor Propellant Grain (Lieske 1989).

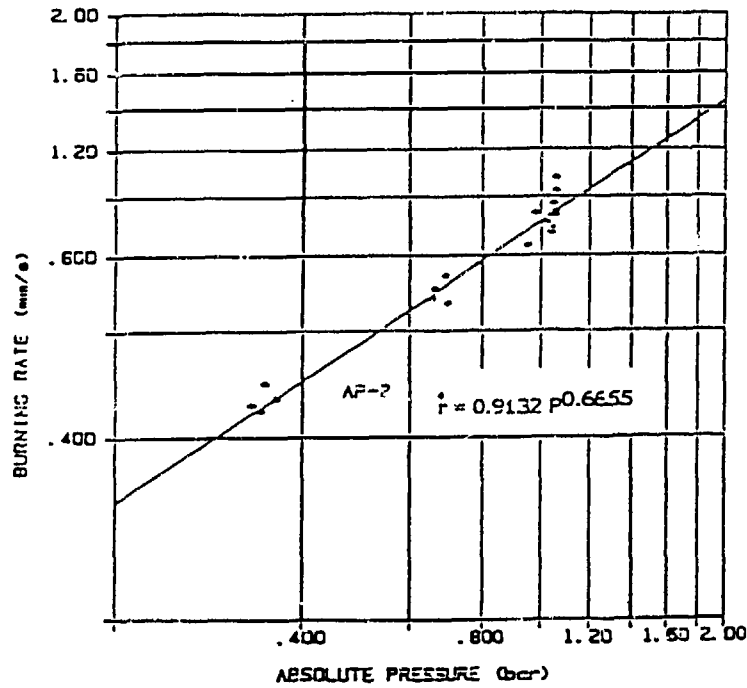


Figure 9. Experimental Strand Burning Rate for M864 Motor Propellant (Miller and Holmes 1987).

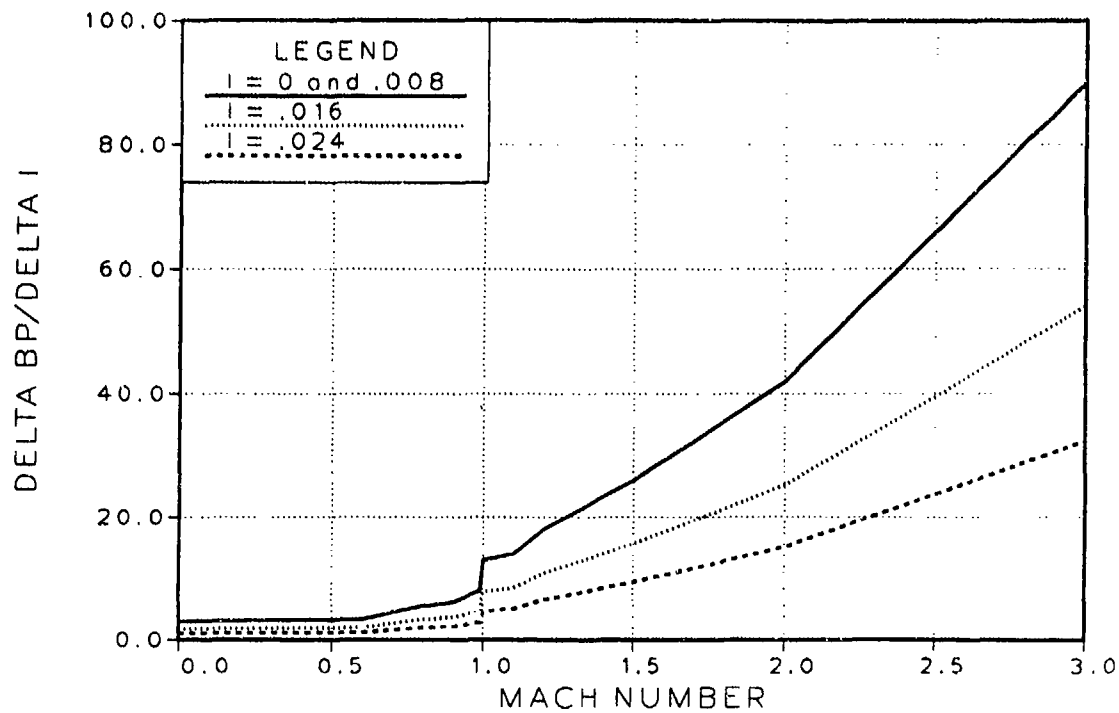


Figure 10. Change in Base Pressure for a Change in Injection Parameter vs. Mach Number and Injection Parameter for the M864 Projectile.

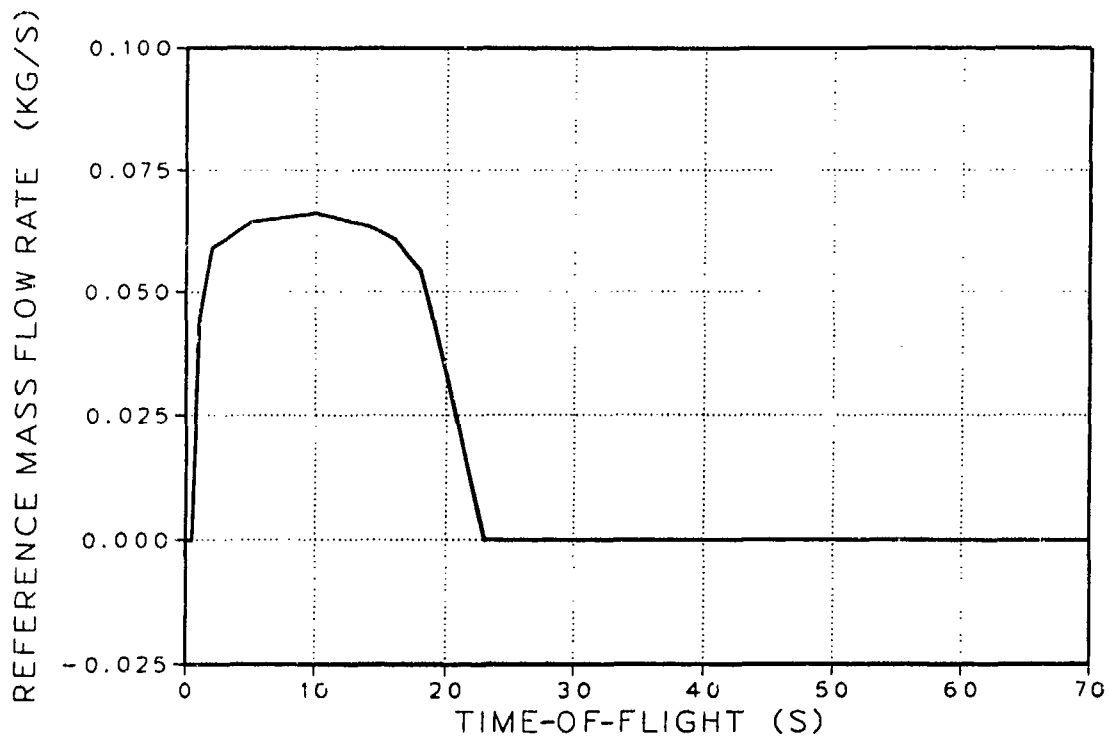


Figure 11. Reference Mass Flow Rate of the Fuel as a Function of the Pseudo-Time-of-Flight for the M864 Motor.

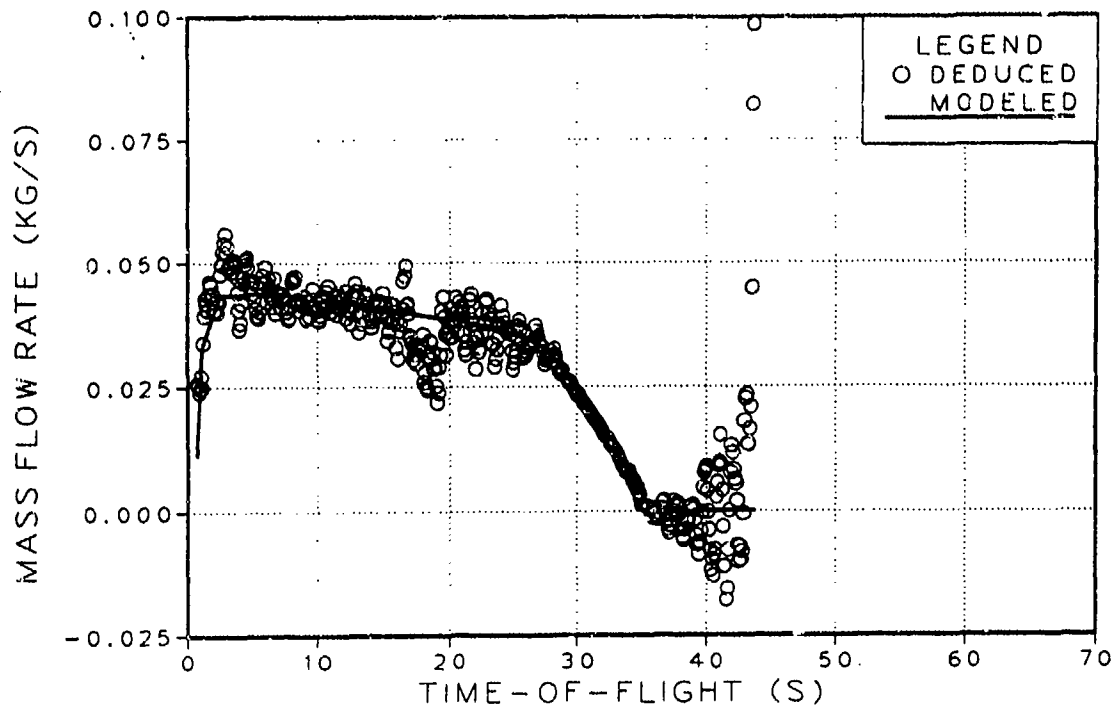


Figure 12. Deduced and Modeled Mass Flow Rate vs. Time-of-Flight for Round Number 5089 Fired with Propelling Charge M4A2, 7W, at a Quadrant Elevation of 500 Mils.

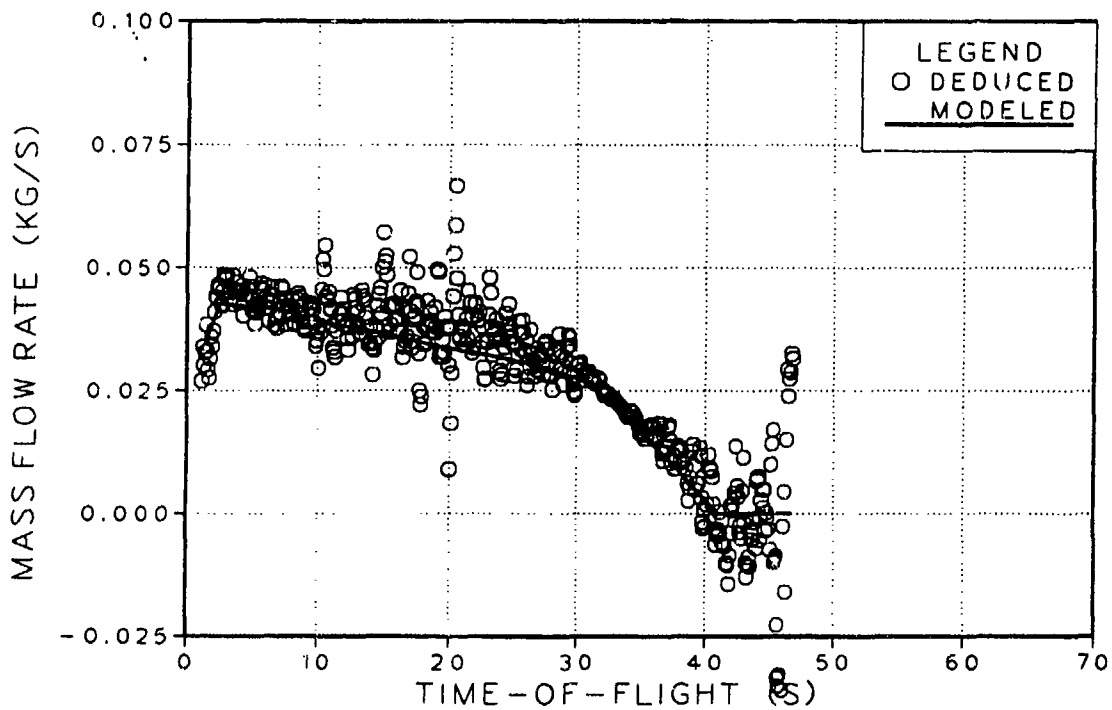


Figure 13. Deduced and Modeled Mass Flow Rate vs. Time-of-Flight for Round Number 1034 Fired with Propelling Charge M4A2, 7W, at a Quadrant Elevation of 750 Mils.

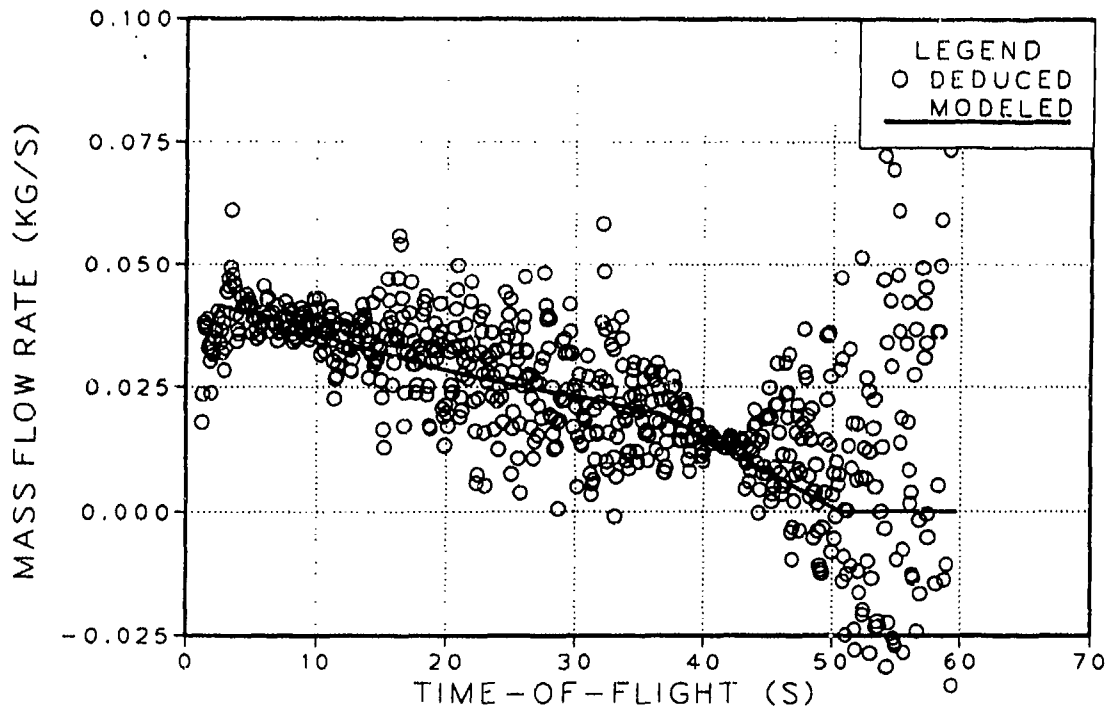


Figure 14. Deduced and Modeled Mass Flow Rate vs. Time-of-Flight for Round Number 1013 Fired with Propelling Charge M4A2, 7W, at a Quadrant Elevation of 1150 Mils.

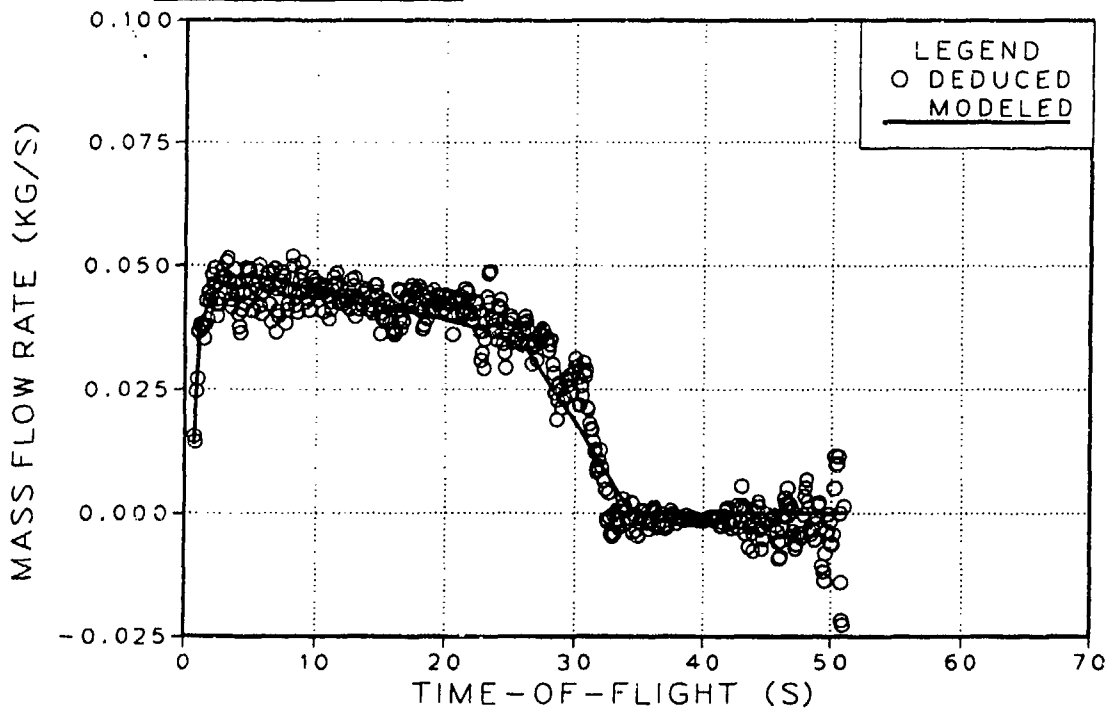


Figure 15. Deduced and Modeled Mass Flow Rate vs. Time-of-Flight for Round Number 1044 Fired with Propelling Charge M119A2, 7R, at a Quadrant Elevation of 500 Mils.

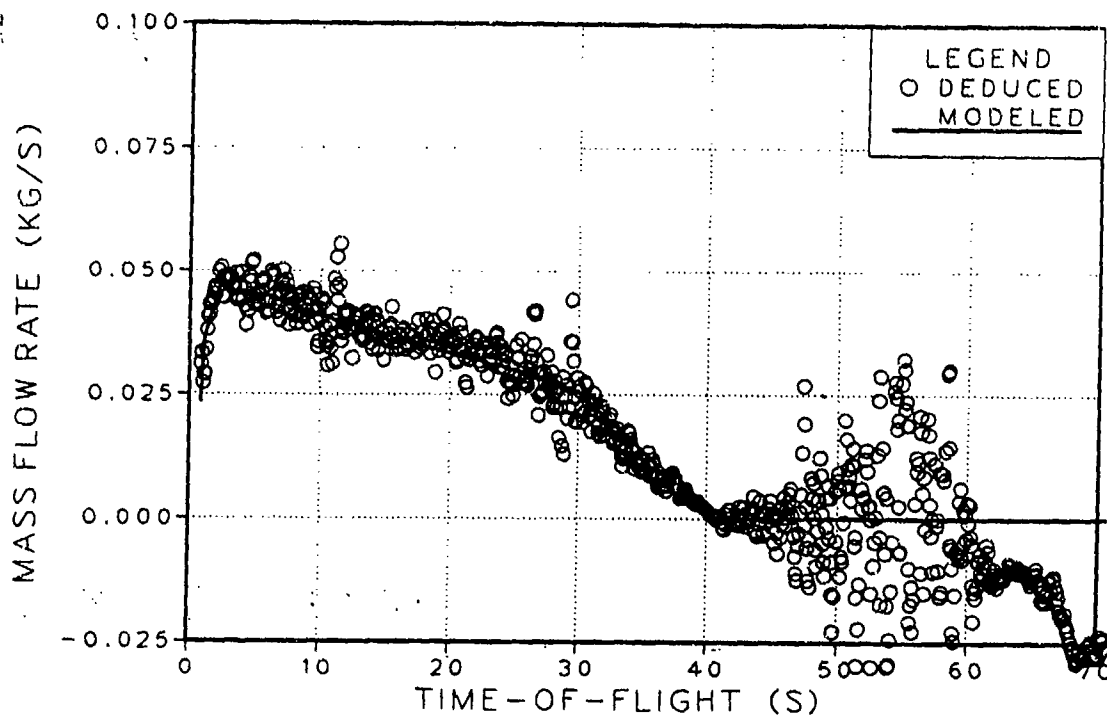


Figure 16. Deduced and Modeled Mass Flow Rate vs. Time-of-Flight for Round Number 1050 Fired with Propelling Charge M119A2, 7R, at a Quadrant Elevation of 750 Mils.

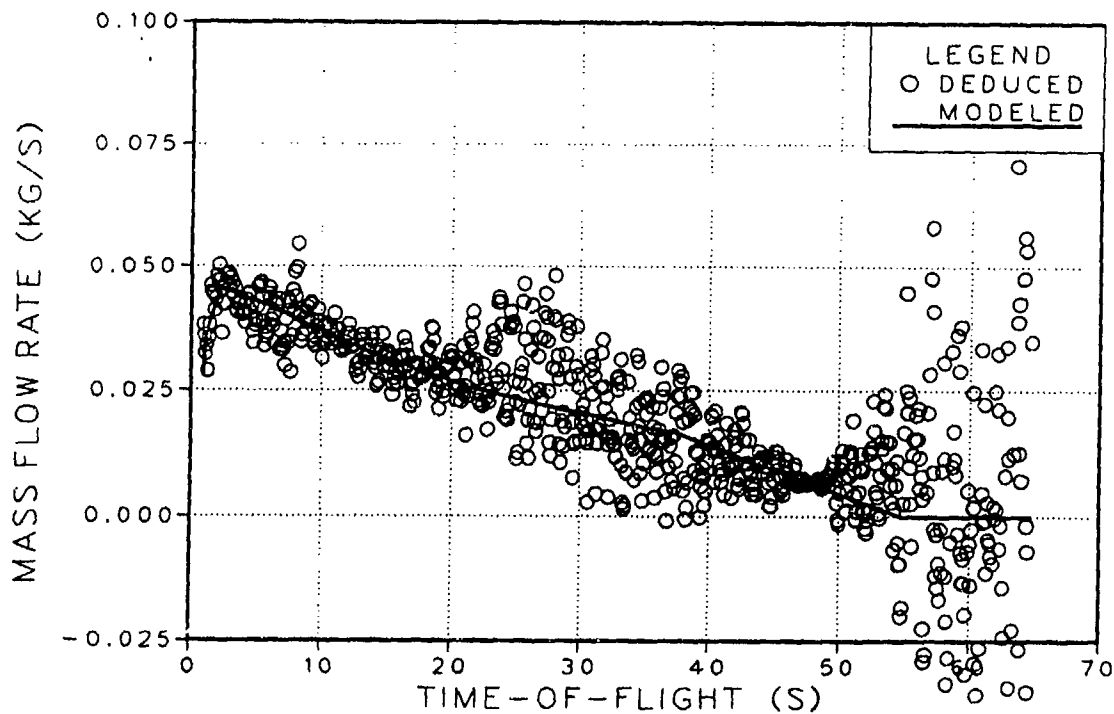


Figure 17. Deduced and Modeled Mass Flow Rate vs. Time-of-Flight for Round Number 4202 Fired with Propelling Charge M119A2, 7R, at a Quadrant Elevation of 1150 Mils.

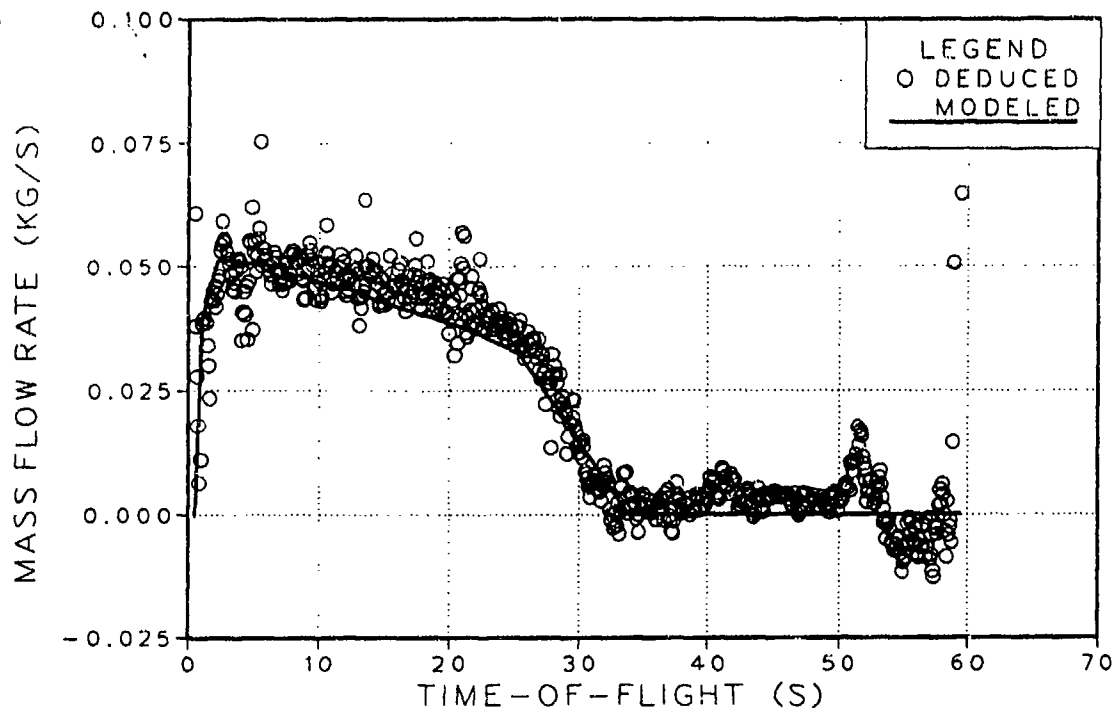


Figure 18. Deduced and Modeled Mass Flow Rate vs. Time-of-Flight for Round Number 4216 Fired with Propelling Charge M203E2, 8R, at a Quadrant Elevation of 499 Mils.

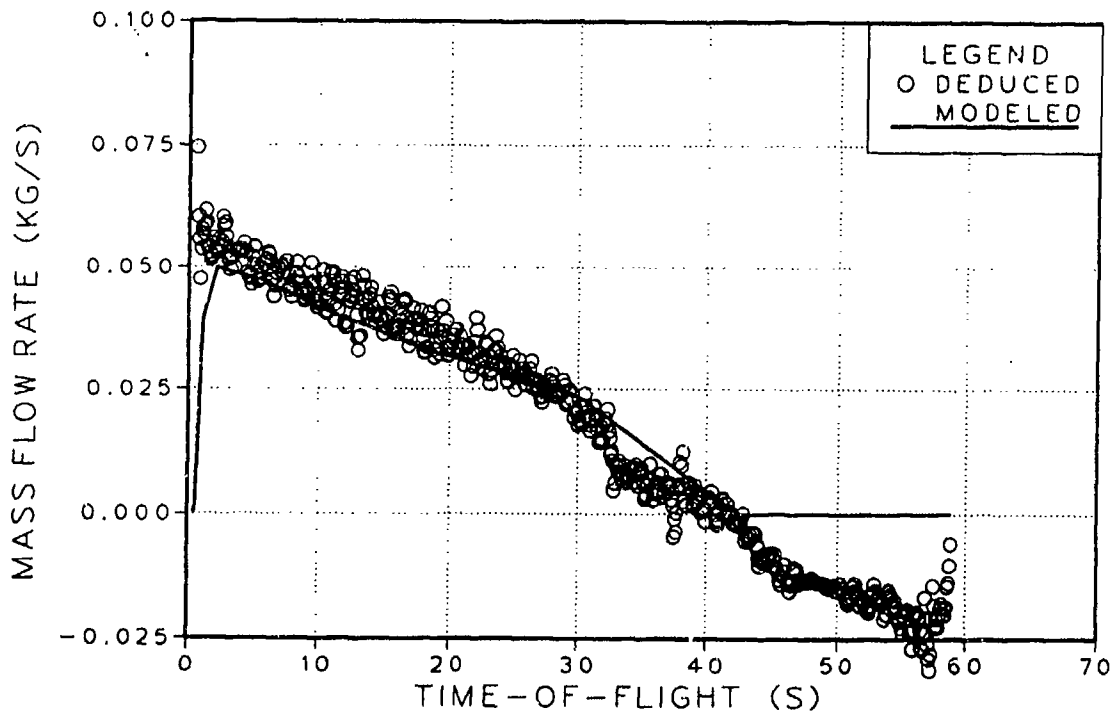


Figure 19. Deduced and Modeled Mass Flow Rate vs. Time-of-Flight for Round Number 4329 Fired with Propelling Charge M203E2, 8R, at a Quadrant Elevation of 748 Mils.

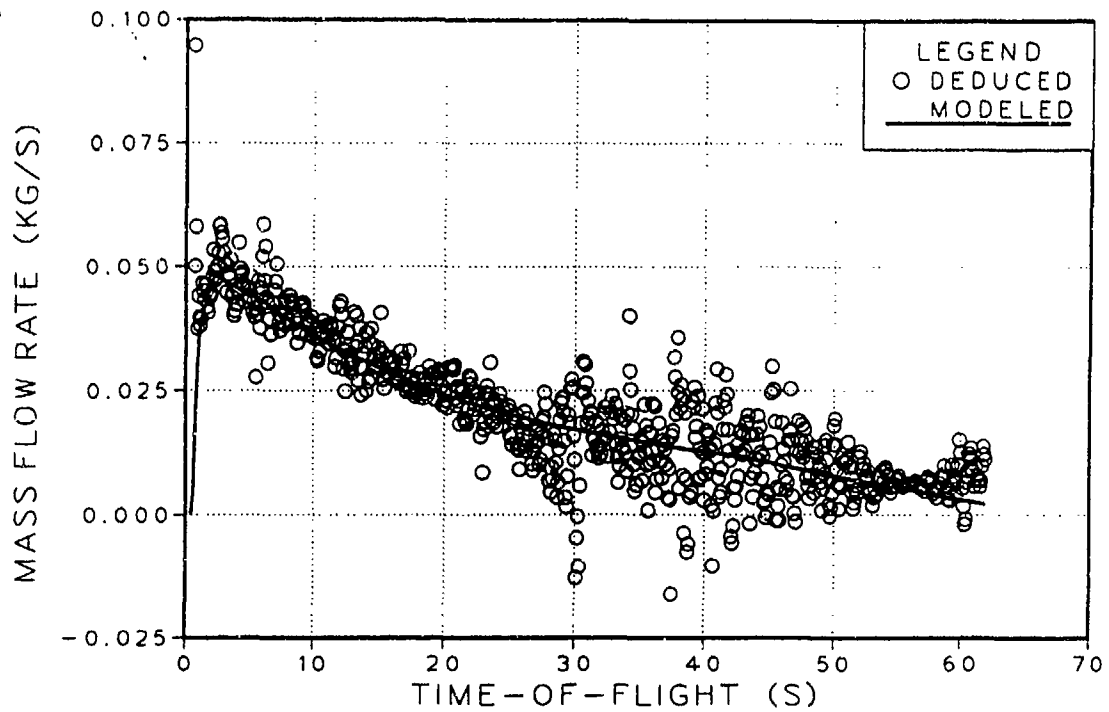


Figure 20. Deduced and Modeled Mass Flow Rate vs. Time-of-Flight for Round Number 4219 Fired with Propelling Charge M203E2, 8R, at a Quadrant Elevation of 1147 Mils.

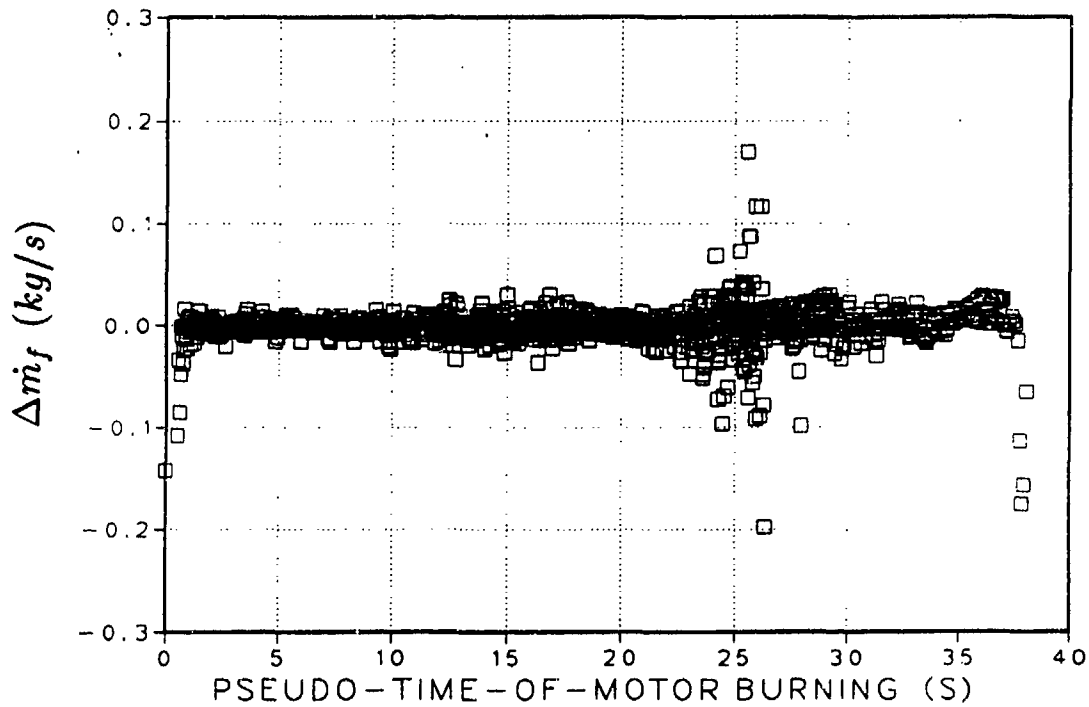


Figure 21. Difference Between Deduced and Modeled Mass Flow Rate (Δm_f) vs. Pseudo-Time-of-Motor Burning.

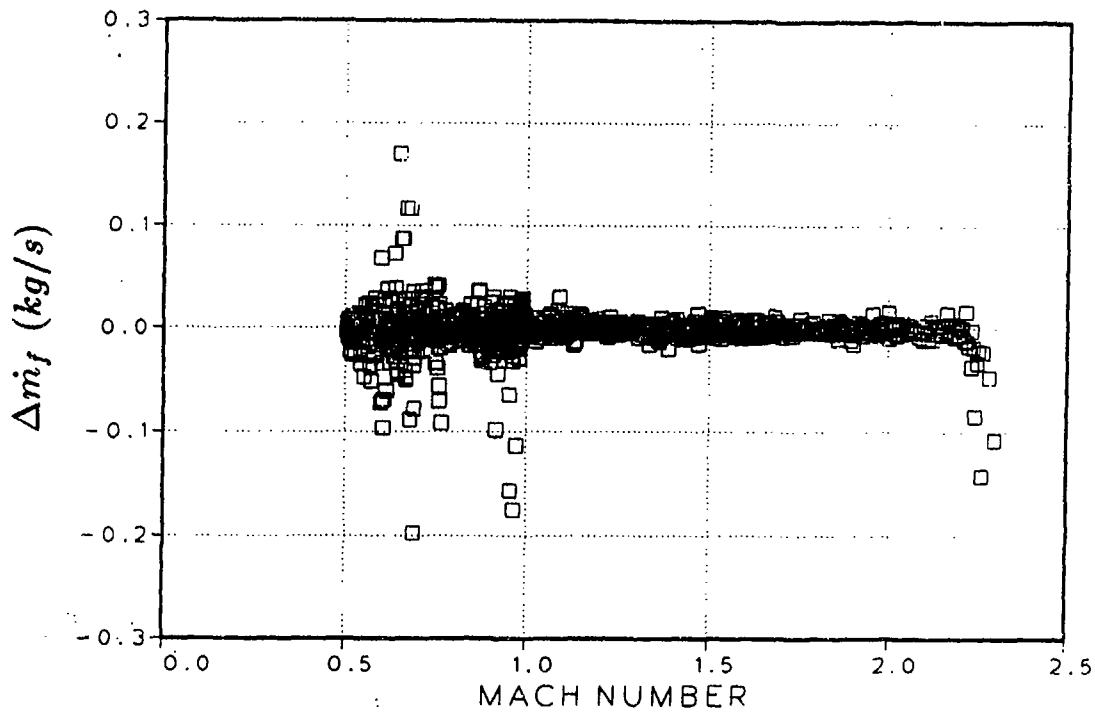


Figure 22. Difference Between Deduced and Modeled Mass Flow Rate ($\Delta \dot{m}_f$) vs. Mach Number.

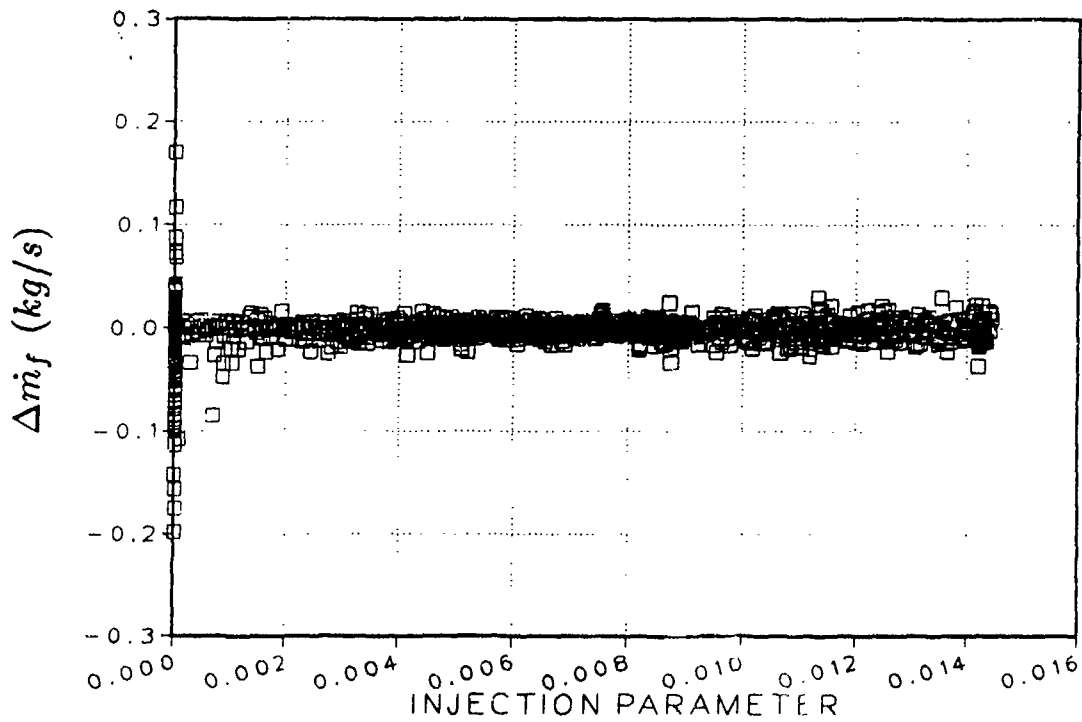


Figure 23. Difference Between Deduced and Modeled Mass Flow Rate ($\Delta \dot{m}_f$) vs. Injection Parameter.

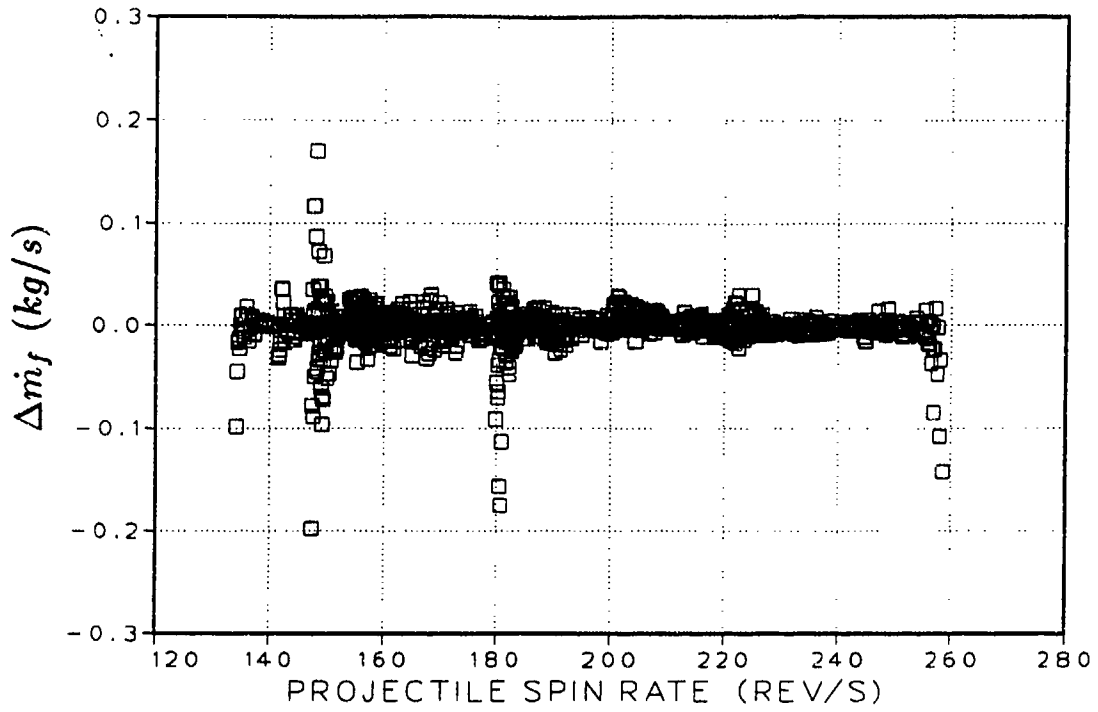


Figure 24. Difference Between Deduced and Modeled Mass Flow Rate (Δm_f) vs. Projectile Spin Rate.

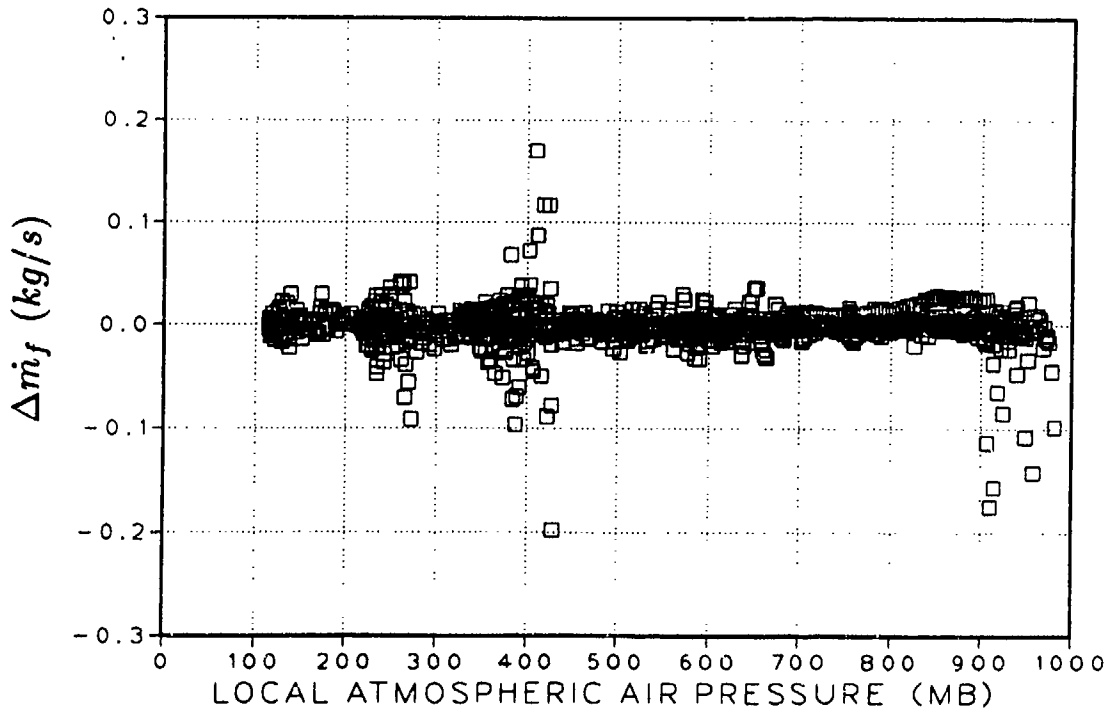


Figure 25. Difference Between Deduced and Modeled Mass Flow Rate (Δm_f) vs. Local Atmospheric Air Pressure.

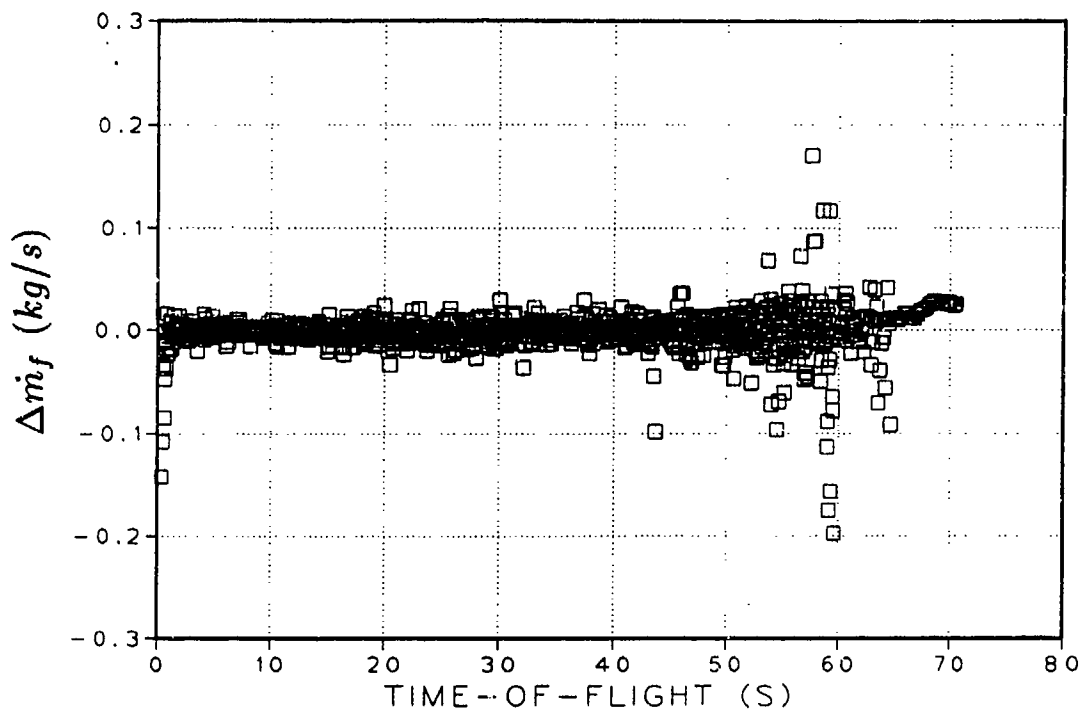


Figure 26. Difference Between Deduced and Modeled Mass Flow Rate ($\Delta \dot{m}_f$) vs. Time-of-Flight.

9. REFERENCES

- Danberg, J.E. "Analysis of the Flight Performance of the 155mm M864 Base Burn Projectile." BRL Report No. 3083, U.S. Army Ballistic Research Laboratory, Aberdeen Proving Ground, MD, April 1990. (AD A222624)
- Gunners, Nils-Erik, Kurt Andersson and Rune Hellgren, National Defense Research Institute (FOA) Tumba, Sweden, "Base-Bleed Systems for Gun Projectiles," Chapter 16, Volume 109, Dated 1988, Progress in Astronautics and Aeronautics, Gun Propulsion Technology, Published by the American Institute of Aeronautics and Astronautics, Inc., 370 L'Enfant Promenade, SW, Washington, DC 20024.
- Kayser, L.D., J.D. Kuzan and D.N. Vazquez. "Ground Testing for Base-Burn Projectile Systems." BRL Memorandum Report No. 3708, U.S. Army Ballistic Research Laboratory, Aberdeen Proving Ground, MD, November 1988. (AD 201107)
- Kuzan, J.D. and V. Oskay. "Ignition Delay of the Solid Propellant in the M864 Base Burn Projectile." BRL Memorandum Report No. 3653, U.S. Army Ballistic Research Laboratory, Aberdeen Proving Ground, MD, March 1988. (AD B121544)
- Lieske, R.F. "Determination of Aerodynamic Drag and Exterior Ballistic Trajectory Simulation for the 155mm, DPICM, M864 Base-Burn Projectile." BRL Memorandum Report No. 3768, U.S. Army Ballistic Research Laboratory, Aberdeen Proving Ground, MD, June 1989. (AD 209510)
- Lieske, R.F. and M.L. Reiter. "Equations of Motion for a Modified Point Mass Trajectory." BRL Report No. 1314, U.S. Army Ballistic Research Laboratory, Aberdeen Proving Ground, MD, March 1966. (AD 485869)
- Miller, M.S. and H.E. Holmes. "An Experimental Determination of Subatmospheric Burning Rates and Critical Diameters for AP/HTPB Propellant." Proceedings of the 1987 JANNAF Combustion Meeting, Monterrey, CA, October 1987.
- NATO Army Armaments Group, Standardization Agreement (STANAG) 4355 (Draft Edition 1), The Modified Point Mass Trajectory Model, February 1988.
- Nietubicz, C.J. and J. Sahu. "Navier-Stokes Computations of Base Bleed Projectiles," Paper No. II-2, First International Symposium on Special Topics in Chemical Propulsion: Base Bleed, Athens, Greece, November 1988.

INTENTIONALLY LEFT BLANK.

LIST OF SYMBOLS

<u>Symbol</u>	<u>Definition</u>	<u>Units</u>
A_b	Total area of the projectile base	m^2
A_e	Exit area of the motor jet	m^2
C_{D_0}	Zero-yaw drag force coefficient	—
$C_{D_{0bb}}$	Drag force coefficient during base-burn motor operation	—
$C_{D_{0T}}$	Zero-yaw drag coefficient during rocket motor burning	—
C_{D_b}	Base drag component	—
C_{D_r}	Radar determined drag force coefficient	—
$C_{D_{\alpha^2}} (Q\alpha_e)^2$	Yaw of repose drag term in the "Modified Point Mass Trajectory Model"	—
$C_{M_\alpha}^*$	Overturning moment coefficient for initially fuzed projectile	—
d	Reference diameter of projectile	m
d_b	Diameter of projectile base	<i>caliber</i>
f_T	Thrust factor	—
f_{BB}	Base-burn factor, used as a parameter for matching experimental range firing data	—
f_{BT_p}	Base-burn motor spin rate burning-time factor	—
f_{BT_P}	Base-burn motor atmospheric air pressure burning-time factor	—
\bar{g}	Acceleration due to gravity	m/s^2
i	Form factor	—
I	Base-burn motor fuel injection parameter	—
I_{SP}	Specific impulse of motor fuel	$N\cdot s/kg$
I_X	Axial moment of inertia of the projectile	$kg\cdot m^2$
I_{X_0}	Axial moment of inertia of the projectile, initially	$kg\cdot m^2$
I_{X_B}	Axial moment of inertia of the projectile at motor burnout	$kg\cdot m^2$
m	Fuzed projectile mass at time t	kg
m_0	Fuzed projectile mass, initially	kg

<u>Symbol</u>	<u>Definition</u>	<u>Units</u>
m_B	Fuzed projectile mass at motor burnout	kg
m_{DI}	Mass of ignition delay element	kg
m_f	Mass of motor fuel, including igniter	kg
\dot{m}_f	Mass flow rate of the motor fuel	kg/s
\dot{m}_f^*	Mass flow rate of the motor fuel as a function of pseudo-time-of-flight	kg/s
M	Local Mach number	—
p	Axial spin rate of projectile	rad/s
p_r	Reference axial spin rate for motor mass flow	rad/s
P	Local atmospheric air pressure	pa
P_b	Average base pressure	pa
P_{bb}	Average base pressure for projectile with an operating base-burn motor	pa
P_{bi}	Average base pressure for projectile with an inert base-burn motor	pa
P_r	Standard atmospheric air pressure at sea level (101325 pa)	pa
r_t	Trajectory estimated, slant range magnitude	m
\vec{r}_t	Trajectory estimated, slant range	m
\dot{r}	HAWK radar determined, rate of change of slant range with time	m/s
\ddot{r}	Time derivative of the HAWK radar determined, slant range rate of change	m/s ²
\dot{r}_t	Trajectory estimated, rate of change of slant range with time	m/s
\ddot{r}_t	Trajectory estimated, time derivative of the slant range range rate of change	m/s ²
t	Time-of-flight	s
t^*	Pseudo-time-of-motor burning	s
t_B	Time-of-motor burnout	s
t_B^*	Reference pseudo-time-of-motor burnout	s

<u>Symbol</u>	<u>Definition</u>	<u>Units</u>
$t_{B(t+\Delta t)}$	Local time-of-motor burnout; varies with time-of-flight due to the change in projectile spin rate and local atmospheric air pressure	s
t_{DI}	Time-of-motor ignition delay	s
t_{DI}^*	Reference pseudo-time-of-motor ignition delay	s
\vec{T}	Acceleration due to motor thrust	m/s ²
\vec{u}_i	Trajectory estimated, velocity of the projectile with-respect-to the ground-fixed axes	m/s
$\dot{\vec{u}}_i$	Trajectory estimated, acceleration of the projectile with-respect-to the ground-fixed axes	m/s ²
\vec{u}_r	Velocity of the projectile with-respect-to the ground-fixed axis, determined from HAWK radar data and estimated trajectory	m/s
$\dot{\vec{u}}_r$	Acceleration of the projectile with-respect-to the ground fixed axes, determined from HAWK radar data and estimated trajectory	m/s ²
v	Speed of projectile with-respect-to air	m/s
\vec{v}	Velocity of the projectile with-respect-to air	m/s
\vec{w}	Velocity of the air with-respect-to the ground (wind velocity)	m/s
X_{CG}	Distance of center of mass of the projectile from nose	m
X_{CG_0}	Distance of center of mass of the projectile from nose, initially	m
X_{CG_B}	Distance of center of mass of the projectile from nose at motor burnout	m
ΔBP	Change in nondimensional base pressure due to the functioning of a base-burn motor	—
$\Delta C_{D_{0_{bb}}}$	Difference between the zero-yaw drag force coefficient for a projectile with an inert and an operating base-burn motor	—
$\Delta \dot{m}_f$	Difference between deduced and modeled mass flow rate	kg/s
Δt	Numerical integration time step size	s
Δt^*	Numerical integration time step size for t^*	s

<u>Symbol</u>	<u>Definition</u>	<u>Units</u>
γ	Ratio of specific heats of air, 1.4	—
$\vec{\Lambda}$	Acceleration due to Coriolis effect	m/s^2
ρ	Local atmospheric air density (specific mass)	kg/m^3
$\frac{\delta BP}{\delta I}$	Change in non-dimensional base pressure for a change in the base-burn motor injection parameter	—
\mathcal{F}	Function of	—

<u>No. of</u> <u>Copies</u>	<u>Organization</u>	<u>No. of</u> <u>Copies</u>	<u>Organization</u>
2	Administrator Defense Technical Info Center ATTN: DTIC-DDA Cameron Station Alexandria, VA 22304-6145	1	Commander U.S. Army Missile Command ATTN: AMSMI-RD-CS-R (DOC) Redstone Arsenal, AL 35898-5010
1	Commander U.S. Army Materiel Command ATTN: AMCAM 5001 Eisenhower Avenue Alexandria, VA 22333-0001	1	Commander U.S. Army Tank-Automotive Command ATTN: ASQNC-TAC-DIT (Technical Information Center) Warren, MI 48397-5000
1	Commander U.S. Army Laboratory Command ATTN: AMSLC-DL 2800 Powder Mill Road Adelphi, MD 20783-1145	1	Director U.S. Army TRADOC Analysis Command ATTN: ATRC-WSR White Sands Missile Range, NM 88002-5502
2	Commander U.S. Army Armament Research, Development, and Engineering Center ATTN: SMCAR-IMI-I Picatinny Arsenal, NJ 07806-5000	(Class. only) 1	Commandant U.S. Army Field Artillery School ATTN: ATSF-CSI Ft. Sill, OK 73503-5000
2	Commander U.S. Army Armament Research, Development, and Engineering Center ATTN: SMCAR-TDC Picatinny Arsenal, NJ 07806-5000	(Uncl. only) 1	Commandant U.S. Army Infantry School ATTN: ATSH-CD (Security Mgr.) Fort Benning, GA 31905-5660
1	Director Benet Weapons Laboratory U.S. Army Armament Research, Development, and Engineering Center ATTN: SMCAR-CCB-TL Watervliet, NY 12189-4050	1	Air Force Armament Laboratory ATTN: WL/MNOI Eglin AFB, FL 32542-5000
(Uncl. only) 1	Commander U.S. Army Armament, Munitions and Chemical Command ATTN: AMSMC-IMF-L Rock Island, IL 61299-5000	2	Dir, USAMSAA ATTN: AMXSY-D AMXSY-MP, H. Cohen
1	Director U.S. Army Aviation Research and Technology Activity ATTN: SAVRT-R (Library) M/S 219-3 Arms Research Center Moffett Field, CA 94035-1000	1	Cdr, USATECOM ATTN: AMSTE-TC
		3	Cdr, CRDEC, AMCCOM ATTN: SMCCR-RSP-A SMCCR-MU SMCCR-MSI
		1	Dir, VLAMO ATTN: AMSLC-VL-D
		10	Dir, BRL ATTN: SLCBR-DD-T

<u>No. of</u> <u>Copies</u>	<u>Organization</u>
1	Commander, TRADOC ATTN: ATAN-AP Fort Monroe, VA 23651-5143
1	Commander TRADOC Analysis Command ATTN: ATRC Fort Leavenworth, KS 66027-5200
1	Commander TRAC-WSMR White Sands Missile Range, NM 88002-5502
2	Commandant U.S. Army Field Artillery School ATTN: ATSF-CCM ATSF-G Fort Sill, OK 73503-5000
1	Director U.S. Army Test and Experimentation Command Fire Support Test Directorate Fort Sill, OK 73503-5000
1	Commander U.S. Army Dugway Proving Ground ATTN: STEDP-MT, Mr. G. C. Travers Dugway, UT 84022
1	Headquarters U.S. Marine Corps ATTN: Code LMW/30 Washington, DC 20380
1	OPM Nuclear ATTN: AMCPM-NUC Picatinny Arsenal, NJ 07806-5000
3	Department of the Army Office of the Product Manager ATTN: SFAE-AR-SD, MR. D. Griggs SFAE-AR-HIP-IP, Mr. R. DeKleine Mr. R. Kantenwein Picatinny Arsenal, NJ 07806-5000
1	Commander U.S. Army Missile Command ATTN: AMSMI-RD-SS-AT, Mr. B. Walker Redstone Arsenal, AL 35898-5010

<u>No. of</u> <u>Copies</u>	<u>Organization</u>
4	Commander U.S. Army Armament Research, Development, and Engineering Center ATTN: SMCAR-FSA, Mr. R. Botticelli Mr. F. Brody Mr. P. DeMasi SMCAR-FSS, Mr. J. Brooks Picatinny Arsenal, NJ 07806-5000
8	U.S. Army Armament Research, Development, and Engineering Center ATTN: SMCAR-AET, Mr. F. Scerbo Mr. J. Bera SMCAR-AET-A, Mr. R. Kline Mr. S. Kahn Mr. F. Brown Mr. H. Hudgins Mr. J. Grau SMCAR-AST, Dr. J. Rubin Picatinny Arsenal, NJ 07806-5000
1	Commander U.S. Army Armament, Munitions, and Chemical Command ATTN: AMSMC-PDC, Mr. L. Randol Rock Island, IL 61299-5000
1	United States Military Academy Department of Mechanics ATTN: LTC A. L. Dull West Point, NY 10996
1	Commander U.S. Naval Warfare Center ATTN: Dr. F. Moore Dahlgren, VA 22448
3	Commander Naval Surface Warfare Center ATTN: Code R44, Dr. F. Priolo Dr. A. Wardlaw K24, B402-12, Dr. W. Yanta White Oak Laboratory Silver Spring, MD 20903-5000

<u>No. of Copies</u>	<u>Organization</u>	<u>No. of Copies</u>	<u>Organization</u>
1	U.S. Naval Weapons Center Aerothermochemistry Division ATTN: Dr. K. C. Schadow China Lake, Ca 93555	1	Director Sandia National Laboratories ATTN: Mr. A. Hodapp Division 1631 Albuquerque, NM 87185
1	Air Force Armament Laboratory ATTN: AFATL/FXA, Mr. S. C. Korn Eglin AFB, FL 32542-5434	1	Director Lawrence Livermore National Laboratory P.O. Box 808 Livermore, CA 94550
2	USAF Wright Aeronautical Laboratories ATTN: AFWAL/FIMG, Mr. N. E. Scaggs Dr. J. Shang WPAFB, OH 45433-6553	1	Georgia Institute of Technology School of Aerospace Engineering ATTN: Dr. W. C. Strahle Atlanta, GA 30332
1	Arnold Engineering Development Center Calspan Field Service ATTN: MS 600, Dr. J. Benek Tullahoma, TN 37389	1	Florida State University Department of Mechanical Engineering ATTN: Dr. W. L. Chow Tallahassee, FL 32316-2175
4	Director National Aeronautics and Space Administration Langley Research Center ATTN: Tech Library Mr. D. M. Bushnell Dr. M. J. Hensch Dr. I. E. Beckwith Langley Station Hampton, VA 23665	1	Massachusetts Institute of Technology ATTN: Tech Library 77 Massachusetts Ave. Cambridge, MA 02139
5	Director National Aeronautics and Space Administration Ames Research Center ATTN: MS-227-8, Mr. L. Schiff MS-258-1, Mr. T. Holst Mr. D. Chaussee Mr. M. Rai MS-229-1, Mr. M. Rubesin Moffett Field, CA 94035	1	Pennsylvania State University Department of Aerospace Engineering ATTN: Dr. G. S. Dulikravich University Park, PA 16802
		1	Pennsylvania State University Department of Mechanical Engineering ATTN: Dr. K. Kuo University Park, PA 16802
		1	The University of Arizona Aerospace Engineering Department ATTN: Prof. I. Wygnanski Tucson, AZ 85721
2	Director Sandia National Laboratories ATTN: Dr. W. L. Oberkampf Dr. F. Blotner Division 1556 P.O. Box 5800 Albuquerque, NM 87185	2	University of California, Davis Department of Mechanical Engineering ATTN: Prof. H. A. Dwyer Prof. J. Steger Davis, CA 95616
		1	University of Cincinnati Department of Aerospace Engineering ATTN: Prof. S. Rubin Mail Location 70 Cincinnati, OH 45221

<u>No. of</u> <u>Copies</u>	<u>Organization</u>
1	University of Illinois at Urbana Champaign Dept. of Mechanical and Industrial Engineering Urbana, IL 61801
2	University of Delaware Department of Mechanical Engineering ATTN: Dr. J. Meakin, Chairman Dr. B. Sidel Newark, DE 19716
1	University of Maryland Department of Aerospace Engineering ATTN: Dr. J. D. Anderson, Jr. College Park, MD 20742
1	University of Notre Dame Dept. of Aeronautical and Mechanical Engineering ATTN: Prof. T. J. Mueller Notre Dame, IN 46556
1	University of Texas Department of Aerospace Engineering and Engineering Mechanics ATTN: Dr. D. S. Dolling Austin, TX 78712-1055
1	Virginia Polytechnic Institute and State University Department of Aerospace and Ocean Engineering ATTN: Dr. C. H. Lewis Blacksburg, VA 24601
1	Applied Technology Associates ATTN: Mr. R. J. Cavalleri P.O. Box 19434 Orlando, FL 32814
1	Arrow Tech Associates, Inc. ATTN: Mr. R. Whyte P.O. Box 4218 South Burlington, VT 05401-0042
3	David Taylor Research Center ATTN: Dr. P. S. Granville Dr. de los Santos Mr. S. Gottlieb Bethesda, MD 20084
2	Ford Aerospace and Communications Corporation Aeronutronics Division ATTN: Mr. C. White Mr. B. Blair

<u>No. of</u> <u>Copies</u>	<u>Organization</u>
	Ford Road Newpoint Beach, CA 92658
2	Alliant Techsystems, Inc. ATTN: Mr. W. E. Martwick Mr. K. Sundeen 600 Second Street, North East Hopkins, MN 55343
2	Morton Thiokol, Inc. Elkton Division ATTN: Mr. J. W. Powers Mr. B. Brooks P.O. Box 241 Elkton, MD 21921-0241
2	Scientific Research Associates ATTN: Dr. H. Gibeling Dr. R. Buggeln 50 Nye Road, P.O. Box 1058 Glastonbury, CT 06033
1	Talley Industries Talley Defense Systems ATTN: Mr. C. R. Huskey 3500 N. Greenfield Road P.O. Box 849 Mesa, AZ 85211
	<u>Aberdeen Proving Ground</u>
2	Dir, USAMSAA ATTN: AMXSY-RA, Mr. R. Scungio AMXSY-GS, Mr. B. King
2	Cdr, USATECOM ATTN: AMSTE-TO-F AMSTE-TE-F, Mr. W. Vomocil
1	PM-SMOKE, Bldg. 324 ATTN: AMCPM-SMK-M, Mr. J. Callahan
1	Dir, USAHEL ATTN: SLCHE-FT
1	Cdr, USACSTA ATTN: STECS-AS-H STECS-EN-B

<u>No. of Copies</u>	<u>Organization</u>	<u>No. of Copies</u>	<u>Organization</u>
1	Ecole Royale Militaire ATTN: Prof. E. Celens Avenue de la Renaissance 30, 1040 Bruxelles, BELGIUM	2	Technical Research and Development Institute Department of Ground Systems Development ATTN: LTG I. Nakatomi COL T. Matsuura 1-2-24, Ikejiri, Setagaya-Ku Tokyo 154 JAPAN
1	Proof and Experimental Test Establishment ATTN: Mr. L.W. Desfosses P.O. Box 2220 Nicolet, Quebec JOG 1EO CANADA	1	MOD ITALY ATTN: Ltc. D. Spada Terrarmimuni Via XX Settembre ITALY
1	Haerens Artilleriskole ATTN: Mr. F.H. Rhe Hansen Postboks 182 DK-6800 Varde DENMARK	1	MOD RNLA, DMKL Test Department ATTN: Ltc. P.L.M. Snel P.O. Box 90822 2509 LV The Hague NETHERLANDS
3	Establissement Technique de Bourges ATTN: Mr. D. Chargelegue Mr. Y. Runfola Ms. O. Donnaud BP 712 18015 Bourges Cedex FRANCE	1	FFI ATTN: Col. D. Cappelen P.O. Box 25 N-2007 Kjeller NORWAY
1	BWB-WM II 6 ATTN: Mr. V. Buehner Konrad Adenauer Ufer 2-6 54 Koblenz GERMANY	1	DGAM ATTN: Mr. J.L. Perez Minguez Poligono de Experiencias Paseo de Extremadura 28024 Madrid SPAIN
1	WTD 91 D. BW-031 ATTN: Mr. D. Haak 4470 Meppen GERMANY	2	National Defence Research Institute Department 2 (FOA 022) ATTN: Dr. K. Andersson Dr. N-E. Gunnars Fack, 104 50 Stockholm SWEDEN
2	Rheinmetall GmbH ATTN: Dr. H. Schilling Dr. L. Borngen Ulmen Strasse 125, D-4000 Dusseldorf 30, GERMANY	2	Swedish Ordnance Guns and Ammunition Division ATTN: Dr. U. Melhus Dr. T. Wik Karlskage S-69180 Bofors SWEDEN
1	TECHNION Aeronautical Engineering Department ATTN: Dr. A. Sigal Haifa 32 000 ISRAEL		

No. of
Copies Organization

- 1 K.K.K. GN.P.P.
ATTN: MAJ A. Durusu
Ankara
TURKEY

- 2 Defence Research Agency
Military Division
ATTN: Mr. D. H. Walker
Mr. C. J. Hilderbrands
Fort Halstead
Sevenoaks, Kent, TN14 7BP
UNITED KINGDOM

USER EVALUATION SHEET/CHANGE OF ADDRESS

This laboratory undertakes a continuing effort to improve the quality of the reports it publishes. Your comments/answers below will aid us in our efforts.

1. Does this report satisfy a need? (Comment on purpose, related project, or other area of interest for which the report will be used.) _____

2. How, specifically, is the report being used? (Information source, design data, procedure, source of ideas, etc.) _____

3. Has the information in this report led to any quantitative savings as far as man-hours or dollars saved, operating costs avoided, or efficiencies achieved, etc? If so, please elaborate. _____

4. General Comments. What do you think should be changed to improve future reports? (Indicate changes to organization, technical content, format, etc.) _____

BRL Report Number BRL-TR-3321 Division Symbol _____

Check here if desire to be removed from distribution list. _____

Check here for address change. _____

Current address: Organization _____
Address _____

DEPARTMENT OF THE ARMY
Director
U.S. Army Ballistic Research Laboratory
ATTN: SLCBR-DD-T
Aberdeen Proving Ground, MD 21005-5066



NO POSTAGE
NECESSARY
IF MAILED
IN THE
UNITED STATES

OFFICIAL BUSINESS

BUSINESS REPLY MAIL
FIRST CLASS PERMIT No 0001, APG, MD

Postage will be paid by addressee.

Director
U.S. Army Ballistic Research Laboratory
ATTN: SLCBR-DD-T
Aberdeen Proving Ground, MD 21005-5066

